

## **Discontinuity in Equilibrium Wave–Current Ripple Size and Shape and Deep cleaning associated with Cohesive Sand–Clay Beds**

X. Wu<sup>1</sup>, R. Fernández<sup>1</sup>, J. H. Baas<sup>2</sup>, J. Malarkey<sup>1,2</sup>, and D. R. Parsons<sup>1</sup>

<sup>1</sup>Energy and Environment Institute, University of Hull, Hull, HU6 7RX, England, U.K.

<sup>2</sup>School of Ocean Sciences, Bangor University, Menai Bridge, LL59 5AB, Wales, U.K.

Corresponding author: Xuxu Wu ([x.wu@hull.ac.uk](mailto:x.wu@hull.ac.uk))

Email addresses:

[X.Wu@hull.ac.uk](mailto:X.Wu@hull.ac.uk)

[R.Fernandez@hull.ac.uk](mailto:R.Fernandez@hull.ac.uk)

[J.Baas@bangor.ac.uk](mailto:J.Baas@bangor.ac.uk)

[J.Malarkey@bangor.ac.uk](mailto:J.Malarkey@bangor.ac.uk)

[D.Parsons@hull.ac.uk](mailto:D.Parsons@hull.ac.uk)

Twitter:

@stickyripple

@icemeanders

@making\_ripples

NA

@bedform

This is a non-peer reviewed preprint submitted to EarthArXiv. The manuscript has been submitted to the *Journal of Geophysical Research: Earth Surface* and is currently under consideration. Feel free to contact any of the authors with queries or to offer constructive feedback.

1           **Discontinuity in Equilibrium Wave–Current Ripple Size and Shape and Deep**  
2           **cleaning associated with Cohesive Sand–Clay Beds**

3           **X. Wu<sup>1</sup>, R. Fernández<sup>1</sup>, J. H. Baas<sup>2</sup>, J. Malarkey<sup>1,2</sup>, and D. R. Parsons<sup>1</sup>**

4           <sup>1</sup>Energy and Environment Institute, University of Hull, Hull, UK.

5           <sup>2</sup>School of Ocean Sciences, Bangor University, Menai Bridge, LL59 5AB, Wales, U.K.

6           Corresponding author: Xuxu Wu ([x.wu@hull.ac.uk](mailto:x.wu@hull.ac.uk))

7           **Key Points:**

- 8           • Ripple growth rates decrease with increasing initial bed clay content in sand-clay  
9           substrates under combined, wave–current, flows.
- 10          • Small, flat ripples occur when the clay content is above an 8% threshold below the ripple  
11          base, as strong cohesion prevents ripple growth.
- 12          • Large clean-sand-like ripples form below the clay threshold, with deep winnowing  
13          (cleaning) of clay and large equivalent clean-sand depths.
- 14

**Abstract**

Sediment mixtures of cohesive clay and non-cohesive sand are widespread in a range of aquatic environments. Ripple dynamics in sand–clay mixtures have been studied under current-alone and wave-alone conditions, but not combined wave–current conditions, despite these conditions being common in estuaries and coastal zone. Here wave–current flume experiments have identified inverse relationships between initial clay content,  $C_0$ , and ripple growth rates and, for the first time, related changing clay contents directly to ripple dimensions during development. There are two distinct types of equilibrium combined-flow ripples in sand–clay mixtures: (a) large asymmetric ripples with dimensions and plan geometries comparable to their clean-sand counterparts for  $C_0 \leq 10.6\%$ ; and (b) small, flat ripples for  $C_0 > 10.6\%$ . The  $C_0 = 10.6\%$  threshold, which may be specific to the experimental conditions, corresponds to a more general 8% threshold found beneath the ripple base, which the clay content must be below for clean-sand dimensions. This ripple-type discontinuity has a three-fold reduction in height, with notable implications for bed roughness. Clay transport rates out of the bed reduced as the ripples developed. For  $C_0 \leq 10.6\%$ , relatively high rates after equilibrium led to clay loss far below the ripple base characterised by large equivalent clean-sand depths, which has not been identified previously. This did not occur for  $C_0 > 10.6\%$ , where clay-loss rates were much lower. In natural environments, this ‘deep cleaning’ may cause concurrent sudden releases of large amounts of pollutants during storms, and reduce post-storm resistance to erosion of sand–clay mixtures.

**Plain Language Summary**

Sticky mud and sand are commonly found in estuaries and across the coastal zone. During storms, the combined effect of waves and currents can erode these sediment beds, creating small undulating ripples. For sand-only beds, ripple size depends on the strength of the waves and currents and the size of the sand grains (fine sand is easier to erode than coarse sand). However,

39 when mud is present, the ripple growth slows down. This study has identified that when waves  
40 and currents are combined: (1) Sediment beds with sand-mud mixtures can form ripples with  
41 similar shapes and sizes as their clean-sand counterparts, where mud is removed from the ripple  
42 and even some ways below it, provided the initial mud content is less than or equal to 10.6%; (2)  
43 Sediment beds with initial mud contents greater than 10.6% cannot be eroded so easily and form  
44 very small ripples that are prevented from growing further due to the stickiness of the mud. While  
45 the 10.6% threshold may be specific to the waves and currents tested, the findings have identified  
46 an important mud-related ripple behaviour which should help to improve the understanding of the  
47 movement of sand and mud in estuaries throughout the world.

## 48 **1 Introduction**

49 Ripples are primary sedimentary structures that are ubiquitous on the bed of estuaries and coastal  
50 seas. These bedforms often preserve information of the flow parameters by which they were  
51 formed (e.g., Southard, 1991, Soulsby and Clarke, 2005). Ripple-related bed roughness in turn  
52 modifies near-bed hydrodynamics and turbulence, ultimately affecting sediment fluxes, a process  
53 which is essential for the modelling of sediment transport (e.g., Soulsby, 1997, Van Rijn, 2007).  
54 Many estuarine and coastal environments face extreme weather events, which are predicted to  
55 increase in frequency with rising sea levels (e.g., Woodruff et al., 2013). Storm-induced waves  
56 combined with currents cause particularly dynamic ripple behaviour, and thus large and rapidly  
57 changing sediment transport rates (e.g., Li and Amos, 1999, Wengrove et al., 2018). The  
58 understanding of how hydrodynamics control ripple dimensions is therefore essential for ensuring  
59 the improved performance of coastal morphodynamic models through well-parameterised bed  
60 roughness. This is also beneficial for the improvement of estuarine and coastal management and  
61 the broader understanding of the impact of climate change and sea level rise on coastal systems.

62 Furthermore, using inverse relationships to predict hydrodynamic variables from ripples preserved  
63 in sedimentary rocks is essential for the accurate reconstruction of paleoenvironments (e.g., Rubin  
64 and Carter, 2005, Myrow et al., 2018). Finally, in view of the nutrient cycle of the coastal  
65 ecosystem, ripples have a significant effect on the exchange of dissolved substances between the  
66 water column and the seabed, providing organic matter to benthic communities and returning the  
67 decompositional products as nitrogen resources for phytoplankton (e.g., Nedwell et al., 1993,  
68 Snelgrove and Butman, 1995, Huettel et al., 1996).

69 Flume studies have provided high-quality process information concerning ripple dynamics on beds  
70 composed of well-sorted clean sand under steady currents (e.g., Baas, 1994, Baas, 1999), waves  
71 (e.g., Pedocchi and García, 2009, O'Hara Murray et al., 2011), and combined wave-current flows  
72 (e.g., Dumas et al., 2005, Perillo et al., 2014b). Empirical formulae developed for the prediction  
73 of ripple size have been derived from clean sand ripples in laboratories and at field sites (e.g.,  
74 Khelifa and Ouellet, 2000, Nelson et al., 2013, Lapotre et al., 2017). However, these ripple size  
75 predictors are of limited use for the majority of estuarine and coastal environments, where  
76 sediment almost universally consists of mixtures of cohesive clay and non-cohesive sand (Healy  
77 et al., 2002). Recently, researchers have therefore focused on ripple dynamics within substrates  
78 composed of mixtures of sand and clay. For steady currents with a depth-averaged velocity of c.  
79 0.36 m/s, Baas et al. (2013) found that equilibrium ripple height decreased with increasing initial  
80 clay content. Wu et al. (2018) highlighted that a small increase in clay content, from 4.2% to 7.4%,  
81 exponentially increased the time needed for ripples to reach equilibrium under waves with a  
82 maximum free stream velocity of c. 0.35 m/s. However, their equilibrium dimensions were  
83 independent of the initial clay content in the bed, up to around 8%. Additionally, clay winnowing,  
84 a hydrodynamic sorting process which suspends the finer clay but leaves the coarser sand in the

85 bed (e.g., Cizeau et al., 1999), played a significant role in the transformation of ripples in mixed  
86 sand–clay to an increasingly sandy composition in the experiments of Baas et al. (2013) and Wu  
87 et al. (2018). Importantly, Baas et al. (2019) have recently highlighted the role of bed cohesion in  
88 decreasing current ripple dimensions in the Dee Estuary, U.K., demonstrating that previous  
89 laboratory findings are applicable in natural environments. There has, however, been very little  
90 research on the dynamics of ripples in mixed sand–clay beds under combined wave–current flows,  
91 which are crucial to the sediment dynamics in the majority of estuaries and coastal seas. This paper  
92 therefore extends the experimental work of Baas et al. (2013) and Wu et al. (2018) by providing  
93 the first results of the influence of cohesive clay on ripple dynamics by means of flume experiments  
94 under combined flows. The three specific objectives were: (1) to quantify ripple development for  
95 different initial bed clay fractions; (2) to determine the relationship between the equilibrium ripple  
96 dimensions and initial bed clay content; and (3) to relate the ripple development to the changing  
97 bed composition, based on quantifying clay winnowing from the bed into the water column.

## 98 **2. Materials and Methods**

### 99 2.1. Experiment Set-up

100 A series of large flume experiments were conducted in the Total Environment Simulator at the  
101 University of Hull. Three channels of equal size (11 m in length and 1.4 m in width, with brick  
102 walls 0.2 m in height) were constructed in a recirculating tank, with a gravel section of one metre  
103 in length at the upstream end to allow for boundary layer development and an artificial beach made  
104 of polyethylene foam at the downstream end to damp out wave reflections (Figure 1a). A cross-  
105 tank mobile gantry centred 3.5 m downstream of the inlet and capable of traversing 2 m  
106 downstream held most of the measurement sensors. A flat sediment bed, 0.1 m thick, was present  
107 in each channel at the start of the experiments. Fresh water was used in all experiments, and the

108 water depth,  $h$ , was set to 0.4 m in the test section. Control Run 1 used three beds of well-sorted  
 109 sand with a median diameter,  $D_{50}$ , of 450  $\mu\text{m}$ . Runs 2 and 3, which considered the effect of physical  
 110 cohesion, used a homogenous mix of kaolinite clay with  $D_{50} = 8.9 \mu\text{m}$  and the same sand. Six beds  
 111 were prepared with initial clay content ranging from 5.7% to 12.3% by dry weight (Table 1).

112 **Table 1. Experimental parameters**

| Run | Duration<br>(min) | Channel* | $C_0$<br>(%) | $U_o$<br>(m/s) | $U_c$<br>(m/s) | $U_{max}$<br>(m/s) | $U_{min}$<br>(m/s) |
|-----|-------------------|----------|--------------|----------------|----------------|--------------------|--------------------|
| 1   | 1970              | 2        | 0            | 0.32           | 0.16           | 0.45               | -0.01              |
| 2   | 2000              | 2        | 10.6         | 0.31           | 0.15           | 0.44               | -0.01              |
|     |                   | 3        | 12.3         | 0.33           | 0.20           | 0.51               | -0.01              |
| 3   | 1250              | 1        | 5.7          | 0.32           | 0.19           | 0.4                | -0.08              |
|     |                   | 2        | 8.5          | 0.31           | 0.16           | 0.45               | -0.01              |
|     |                   | 3        | 11.6         | 0.33           | 0.19           | 0.50               | -0.01              |

113 \* Data for channel 1 of Run 2 is excluded because clay and sand were not mixed  
 114 homogeneously.

115  
 116 Each run was carried out using combined flows. Flow velocities in each channel were measured  
 117 by a 25 Hz Vectrino profiler fixed on the gantry beam 4.5 m away from the flume inlet and at 0.12  
 118 metres above the initial flat bed (Figure 1a). The monochromatic wave height,  $H$ , and wave period,  
 119  $T$  were c. 0.17 m and 2 s, respectively, measured by eight 50 Hz acoustic water level sensors 0.7  
 120 m above the still water surface in the tank (Figure 1b). The wave velocity amplitude at the edge of  
 121 the boundary layer,  $U_o$ , was c. 0.32 m/s, and the depth-averaged current velocity,  $U_c$ , was c. 0.16  
 122 m/s. Although there was a small variation in velocities across the flume tank (Table 1), this did not  
 123 significantly influence ripple evolution. The waves in the experiments were skewed shallow-water  
 124 waves with sharp crests and long troughs, generating a maximum combined flow velocity,  $U_{max}$ ,  
 125 of c. 0.45 m/s and a minimum combined flow velocity,  $U_{min}$ , of c. -0.01 m/s at a height above the  
 126 bed of 0.05 m, when combined with the current (Table 1). Closer to the bed, using the approach

127 of Malarkey and Davies' (2012) strongly non-linear option for calculating the mean bed shear  
 128 stress,  $\tau_m$ , and maximum bed shear stress,  $\tau_{\max}$ , associated with a skin friction roughness of  $2.5D_{50}$   
 129 ( $z_0 = 2.5D_{50}/30$ , where  $z_0$  is the theoretical height of zero velocity) in wave–current flow  
 130 determined from  $h$ ,  $U_o$ ,  $T$  and  $U_c$ , gives  $\tau_{\max} = 1.41$  Pa and  $\tau_m = 0.14$  Pa. The minimum bed shear  
 131 stress,  $\tau_{\min} = \tau_m - \tau_{\max}$ , was  $-1.27$  Pa, indicating that bed shear stress was far more symmetric in  
 132 the two wave half cycles than the velocity higher up in the flow.

133 The non-dimensional Shields parameter is defined by  $\theta = \tau/(\rho_s - \rho)gD_{50}$ , where  $\rho_s$  is the sediment  
 134 density ( $= 2650$  kg/m<sup>3</sup>),  $\rho$  is the water density ( $= 1000$  kg/m<sup>3</sup> for freshwater,  $1027$  kg/m<sup>3</sup> for  
 135 saltwater) and  $g$  is the acceleration due to gravity ( $= 9.81$  m/s<sup>2</sup>). During the intertidal Dee Estuary  
 136 (UK) field deployment of Lichtman et al. (2018) and Baas et al. (2021),  $D_{50} = 0.227$  mm,  $0 < h \leq$   
 137  $3.5$  m,  $0 < U_c \leq 0.6$  ms<sup>-1</sup>,  $0 < U_o \leq 0.45$  ms<sup>-1</sup> and  $0 < C_0 \leq 14\%$ . During a storm event (inundations  
 138 2 to 6 of Lichtman et al. (2018) and Baas et al. (2021)), the peak  $\tau_{\max}$ , calculated in the same way  
 139 as above, varied between  $0.55$  and  $1.69$  Pa and the clean-sand Shields parameter threshold,  $\theta_0$ ,  
 140 according to Soulsby (1997) was  $0.05$ , or  $0.15 \leq \theta_{\max} \leq 0.47$  and  $3 \leq \theta_{\max}/\theta_0 \leq 9$ . For the present  
 141 experiments, the values of  $h$ ,  $U_c$ ,  $U_o$  and  $C_0$  were all within these ranges (Table 1), and since  $\theta_{\max}$   
 142  $= 0.19$ ,  $\theta_0 = 0.03$  and  $\theta_{\max}/\theta_0 \approx 7$ , the shear stress was also within the field range. Thus the  
 143 experimental conditions herein are consistent with intertidal storm conditions in a macrotidal  
 144 estuary.

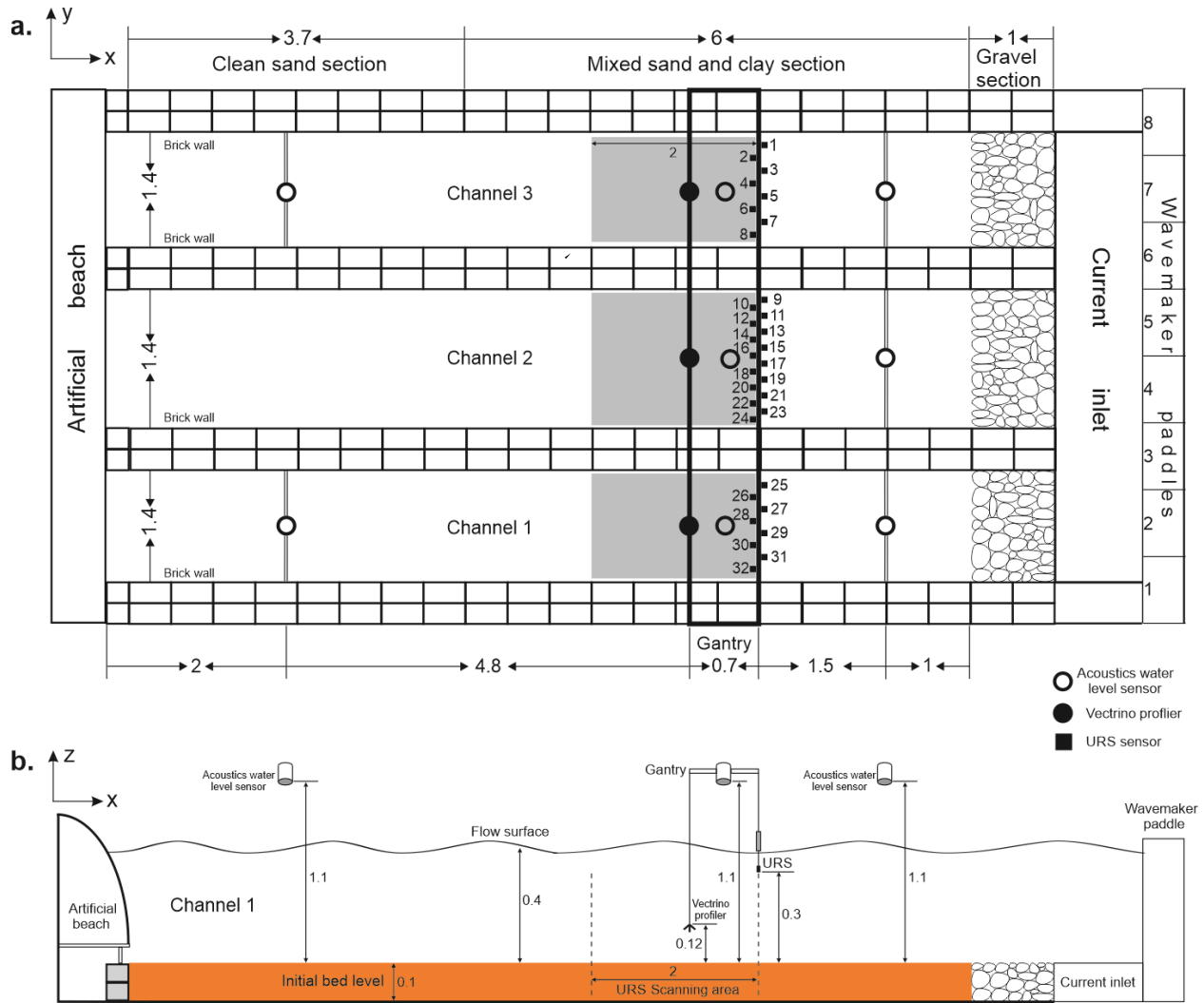


**Figure 1. (a) Plan view and (b) Side view of the experimental set-up. The grey area is scanned by an Ultrasonic Range System (URS) with numbered sensors (black squares). White and black circles denote acoustic water level sensors and Ventrino profilers, respectively. Dimensions are in metres.**

## 2.2. Procedure

The clay was homogeneously mixed into the sand using a handheld plasterer's mixer in each channel, flattened using a wooden leveller, and scanned using a terrestrial 3D laser scanner (FARO Focus3D X330). At the start of each experiment, syringe-type sediment cores with a diameter of 20 mm and a maximum length of 90 mm were collected from six locations at one-metre intervals

155 along the centre lines of the mixed sand–clay sections. A homogenous sand–clay mix was present  
156 in all channels (Figure S1), except for one substrate in Run 2, Channel 1, which was therefore  
157 excluded from the results presented below.

158 Bedform evolution was recorded in three dimensions using a Seatek 2MHz Ultrasonic Ranging  
159 System (URS) mounted on the gantry 4 m downstream of the flume inlet and 0.3 m above the bed.  
160 The URS contained 32 probes spatially distributed across the three channels (16 across Channel 2  
161 and 8 across Channels 1 and 3). During the experiment, the URS probes were static and positioned  
162 3.5 m downstream from the current inlet to monitor ripple migration rate,  $m = n\lambda/t$ , where  $n$  is the  
163 number of ripples migrating below the URS probes over a time period  $t$  ( $t = 60$  min). Additionally,  
164 every time the flow was temporarily stopped, the array scanned the bed over a two-metre length  
165 swathe via an auto-traverse system with a speed of 1 mm/s (Figure 1).

166 Bed scanning was conducted at pre-set time intervals, gradually increasing from a 5-min interval  
167 in the initial phases of the runs, up to 180 min in the later phases of the runs. Sediment syringe  
168 cores from the mixed clay and sand sections were also collected during the experiments whilst the  
169 waves and currents were temporarily stopped. In Run 2, sediment cores were collected at two  
170 locations within the 2-m scan swathe: near the start and near the end. One more collection location  
171 from the middle of the swathe was added in Run 3 because ripples with lower clay content were  
172 expected to develop faster and an additional sampling point was deemed beneficial to quantifying  
173 winnowing. At each collection location, one core was taken from the initial flat bed and, as soon  
174 as ripples were identified with the URS, a core was collected from a crest and a consecutive trough.  
175 After each experiment, the water was drained slowly from the tank and the rippled bed was scanned  
176 with the 3D laser scanner, and sediment cores from neighbouring ripple crests and troughs were  
177 also collected. Additional sediment cores were collected from the ripples in the downstream clean

178 sand section in order to quantify the amount of clay that had re-entered the sandy substrate by  
 179 hyporheic processes. All sediment cores were stored in a cold store at a temperature of 4°C prior  
 180 to grain size analysis using a Malvern Mastersizer 2000. The sediment cores from the initial flat  
 181 bed and from the ripple troughs were sliced in 10-mm intervals for the grain size analysis; the  
 182 cores obtained from the ripple crests were sliced in 5-mm intervals to provide higher resolution of  
 183 the clay content within the ripples.

### 184 2.3. Postprocessing of Data

185 Ripple wavelengths,  $\lambda$ , and heights,  $\eta$ , were determined from the bed elevation profiles (BEP),  
 186 recorded by each URS sensor. The removal of spikes from the raw BEPs was based on  $dz > dz_m$ ,  
 187 where  $dz$  is the vertical distance between consecutive data points in the BEP and  $dz_m$  is the average  
 188 vertical distance in the BEP (Van der Mark et al., 2008). Each BEP was then smoothed using a  
 189 three-point moving average, followed by applying MATLAB® ‘peaks and troughs’ tool to identify  
 190 the locations of ripple crests and troughs. The end-of-experiment cross-sectional shape of the  
 191 ripples was characterized by calculating the ripple steepness (RS) and ripple symmetry index  
 192 (RSI):

$$RS = \eta/\lambda, \quad (1)$$

193

$$RSI = \lambda_s/\lambda_l, \quad (2)$$

194

195 where  $\lambda_s$  and  $\lambda_l$  are the length of the stoss side and lee side, respectively. RSI values between 1 and  
 196 1.3 denote symmetric ripples and RSI values higher than 1.5 denote increasingly asymmetric  
 197 ripples. Ripples are quasi-asymmetric for  $1.3 < RSI < 1.5$  (Perillo et al., 2014a).

198 Furthermore, the mean values of  $\eta_t$  and  $\lambda_t$  at a bed scanning time  $t$  were calculated from all ripples  
 199 in the BEPs in each channel, in order to construct development curves of ripple height and  
 200 wavelength. Equilibrium ripple height,  $\eta_e$ , and wavelength,  $\lambda_e$ , and the time required to reach  
 201 equilibrium height,  $T_\eta$ , and wavelength,  $T_\lambda$ , were calculated using best-fit equations proposed by  
 202 Baas et al. (2013), which include a delay time for the first appearance of ripples on the flat bed,  $t_i$ :

$$\frac{\eta_t - \eta_i}{\eta_e - \eta_i} = 1 - 0.1 \frac{t - t_i}{T_\eta - t_i}, \quad (3)$$

$$\frac{\lambda_t - \lambda_i}{\lambda_e - \lambda_i} = 1 - 0.1 \frac{t - t_i}{T_\lambda - t_i}, \quad (4)$$

203 where  $\eta_e$ ,  $\lambda_e$ ,  $T_\eta$ ,  $T_\lambda$ ,  $\lambda_i$ , and  $t_i$  are fitting coefficients, and  $\lambda_i$  is the initial wavelength of the first  
 204 ripples that appeared on the flat bed in each run. The initial ripple height,  $\eta_i$ , is zero except when  
 205 more than one growth stage is fitted to the data. In this study, the equilibrium time was defined as  
 206 the time taken for the ripple wavelength or height to reach 90% of its equilibrium value (cf., Baas  
 207 et al., 2013). The coefficient  $t_i$  was zero in the control run with clean sand (Table 2). All the fitting  
 208 coefficients for the combined-flow ripples are listed in Table 2 and discussed in section 3. The  
 209 characteristic ripple height growth rate,  $r_\eta$ , and wavelength growth rate,  $r_\lambda$ , over the experiment  
 210 were estimated as follows:

$$r_\eta = \eta_e / T_\eta, \quad (5)$$

$$r_\lambda = (\lambda_e - \lambda_i) / T_\lambda. \quad (6)$$

211  
 212 Assuming that these rates are small compared to the ripple migration rate,  $m$ , which will be  
 213 demonstrated later, the rate of removal of clay out of the bed does not have to take changes in  
 214 ripple dimensions into account. The total amount of clay removed since the beginning of the  
 215 experiment,  $I$ , can be estimated by:

$$I = \int_{-b}^0 w C_d dz, \quad (7)$$

216 where  $z = 0$  and  $z = -b$  correspond to the ripple crest and the lowest reference levels of the sediment  
 217 cores, respectively,  $C_d(z)$  is the clay deficit in the bed, compared to  $C_0$ , given by  $C_d = C_0 - C$ , and  
 218  $C$  is the measured clay content in the sediment cores, such that  $I = 0$  for the initial core by  
 219 definition. The weighting function  $w(z) = -z/\eta$ , for the active layer ( $-\eta < z < 0$ ), and  $w(z) = 1$  for  $z$   
 220  $\leq -\eta$  and  $z = -\eta$  corresponds to the ripple trough depth (the vertical offset for the trough core).  
 221 The weighting function represents the fraction of the bed taken up by the ripple assuming it has a  
 222 triangular cross section. Equation (7) also allows for the definition of an equivalent clean-sand  
 223 depth  $d_c = I/C_0$ , which is the effective depth to which clay has been removed. This quantity can be  
 224 compared to the ripple height.

225 The mass transport rate of clay per unit width out of the bed,  $T_b$ , was determined by:

$$T_b = (1 - p)\rho_s\lambda\frac{\Delta I}{\Delta t}, \quad (8)$$

226 where  $p = 0.4$  is the closest packing porosity, and  $\Delta I$  and  $\Delta t$  are the changes in  $I$  and time,  $t$ , between  
 227 sequential cores.

228 Finally, in order to characterise its behaviour, the clay concentration in the bed is fitted to a  
 229 Gaussian type function:

$$C(z) = \begin{cases} C_s, & -z_s \leq z < 0, \\ C_0 - (C_0 - C_s)\exp[-\alpha(z + z_s)^2], & -b \leq z < -z_s, \end{cases} \quad (9)$$

230 where  $C_s$  is the clay concentration at the surface,  $z_s$  is the height above which the clay concentration  
 231 is constant ( $z_s \leq \eta$ ),  $\alpha$  is the decay constant and  $b$  is set to a fixed depth of 100 mm for all profiles.

232 **3. Results**

## 233 3.1. Ripple Development

234 During the control run ( $C_0 = 0\%$ ), small ripples appeared on the flat bed immediately after the  
 235 hydrodynamic forcing was applied, as evidenced by a five-min period of rapid growth, during  
 236 which the ripple wavelength and height reached 88.1 mm and 7.2 mm, respectively. Thereafter,  
 237 the ripple growth rate progressively declined until the ripples stabilised (Figure 2a, b). The  
 238 development of these ripples exhibited a general trend similar to that reported in the combined-  
 239 flow experiments of Perillo et al. (2014b). Equations 3 and 4 revealed that the ripples took 90 min  
 240 and 170 min to reach an equilibrium height and wavelength of 14.6 mm and 123.6 mm,  
 241 respectively, with high fit confidence of 0.94 and 0.78 (Figure 2a, b; Table 2). These fully  
 242 developed ripples were two-dimensional in planform geometry, characterised by straight,  
 243 continuous ripple crestlines (Figure 3a). The majority of the ripples was symmetric or quasi-  
 244 asymmetric, with a ripple symmetry index (RSI) of 1.4 and a ripple steepness (RS) of 0.12 (Table  
 245 2), indicating that they were similar to wave-generated vortex ripples (Miller and Komar, 1980).

246

247 **Table 2. Ripple parameters**

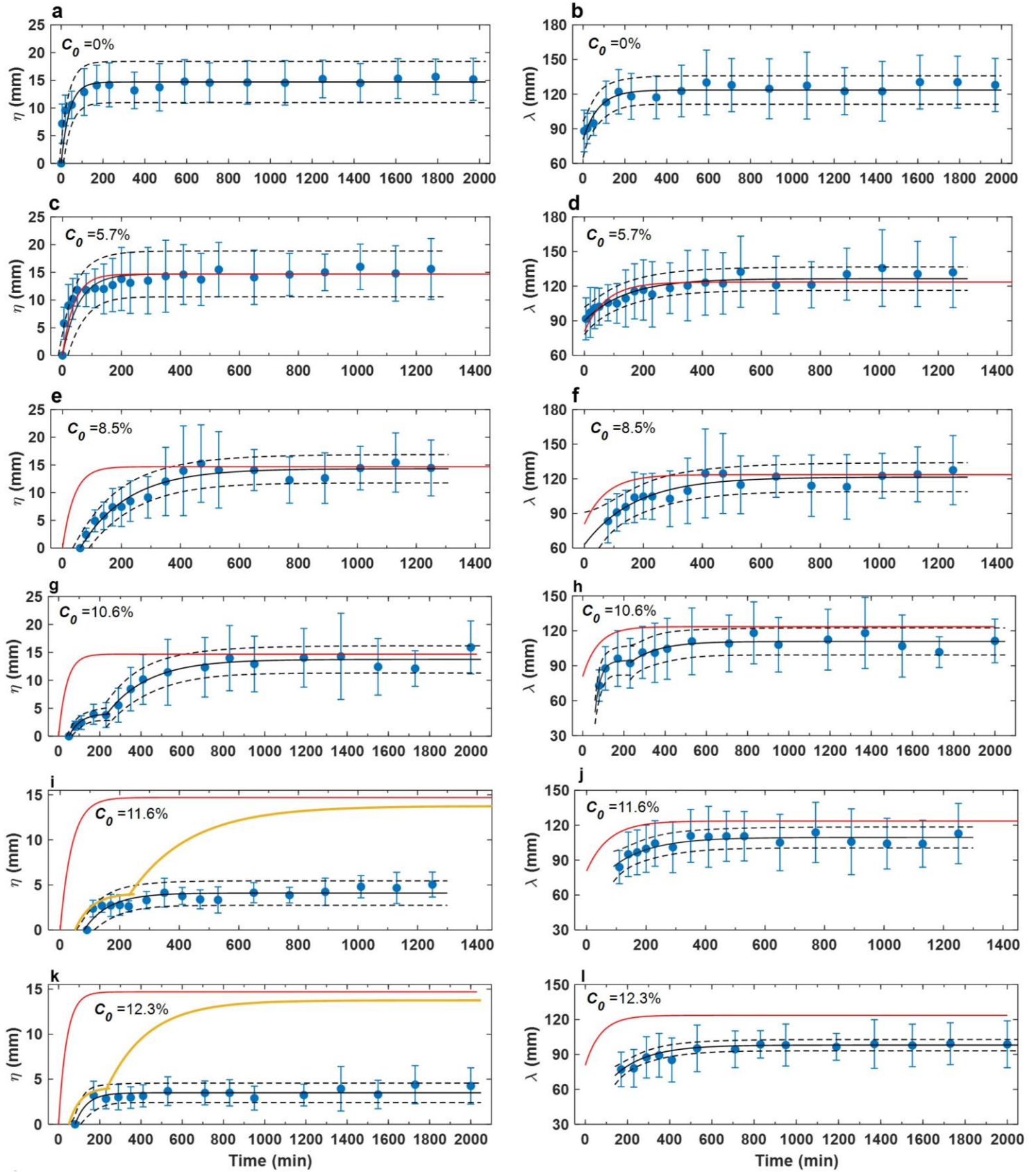
| Run | Channel | $C_0$<br>(%) | $\eta_e$<br>(mm) | $T_\eta$<br>(min) | $r^2$<br>(-) | $\lambda_e$<br>(mm) | $\lambda_i$<br>(mm) | $T_\lambda$<br>(min) | $r^2$<br>(-) | $t_i$<br>(min) | RSI<br>(-) | RS<br>(-) |
|-----|---------|--------------|------------------|-------------------|--------------|---------------------|---------------------|----------------------|--------------|----------------|------------|-----------|
| 1   | 2       | 0            | 14.4±1.8         | 90                | 0.78         | 123.6±4.9           | 80.7±10.8           | 170                  | 0.94         | -              | 1.4±0.3    | 0.12±0.02 |
| 2   | 2       | 10.6         | 13.7±1.0*        | 678*              | 0.92         | 110.9±4.0*          | 92.6±10.2*          | 540*                 | 0.63         | 60*            | 1.3±0.3    | 0.14±0.03 |
|     | 3       | 12.3         | 3.5±0.3          | 211               | 0.79         | 98.0±1.7            | 71.7±6.3            | 499                  | 0.93         | 120            | 1.5±0.5    | 0.04±0.02 |
| 3   | 1       | 5.7          | 14.7±1.1         | 125               | 0.74         | 126.5±3.5           | 91.3±6.3            | 330                  | 0.88         | 5              | 1.4±0.3    | 0.12±0.02 |
|     | 2       | 8.5          | 14.3±1.0         | 432               | 0.96         | 121.4±5.1           | 80.2±11.6           | 456                  | 0.85         | 60             | 1.4±0.3    | 0.11±0.02 |
|     | 3       | 11.6         | 4.1±0.4          | 271               | 0.76         | 108.5±2.6           | 84.5±10.            | 382                  | 0.78         | 90             | 1.5±0.5    | 0.05±0.02 |

248

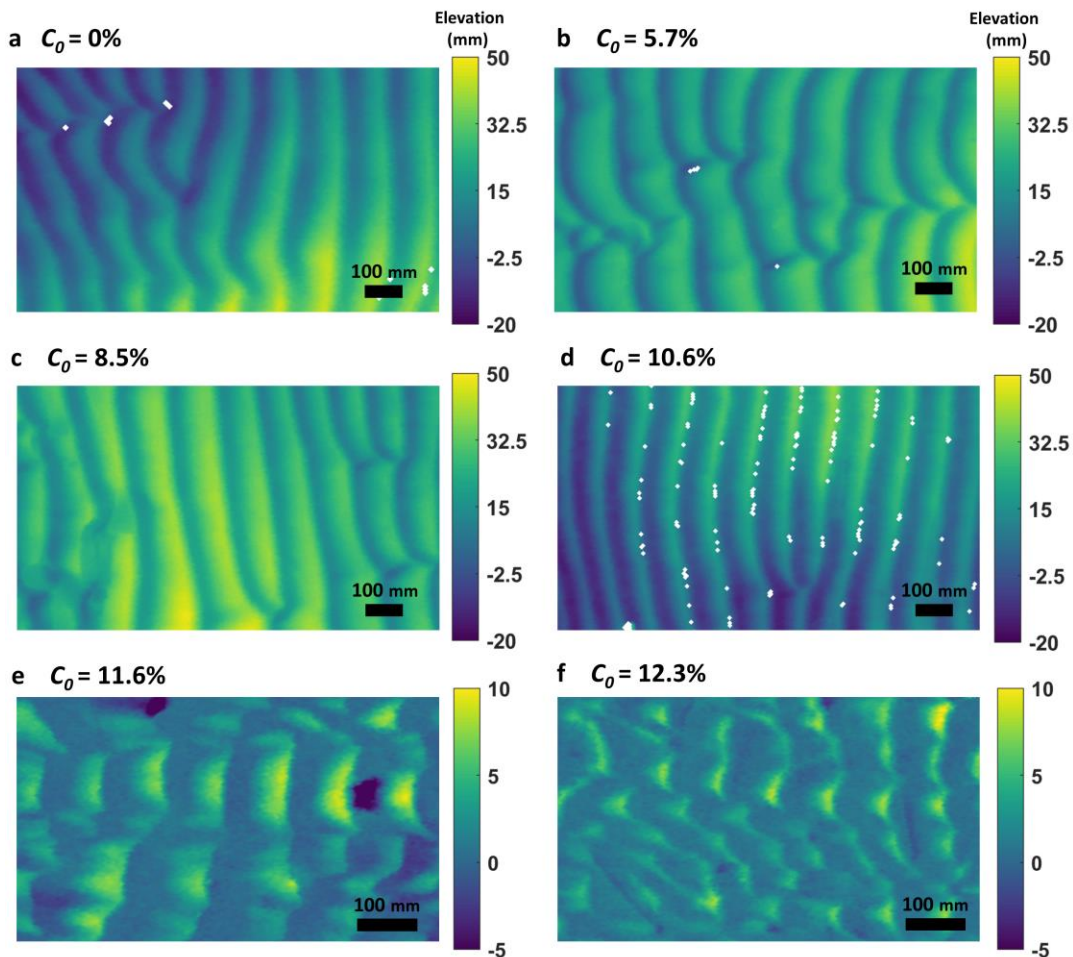
249  $r^2$ : Squared correlation coefficient of the best fit curve.

250  $\pm$ : Standard deviation.

251 \* Based on a two-stage fitting (first stage for  $t \leq 230$  min, with  $\eta_i = 0$  mm and  $\lambda_i = 46$  mm; second  
252 stage for  $t > 230$  min, with  $\eta_i = 3.8$  mm and  $\lambda_i = 92.6$  mm, the quoted value of  $T_\eta$  and  $T_\lambda$  includes  
253 the time of the first stage, 230 min).



255 **Figure 2. Development trends for (a, c, e, g, i, and k) ripple height and (b, d, f, h, j, and**  
 256 **l) ripple wavelength. Blue vertical lines denote one standard deviation of the mean**  
 257 **dimension. Black lines are based on fitting to equations 3 and 4. Red and yellow**  
 258 **lines are best-fit curves for clean-sand and 10.6% cases, for comparison. Black dash**  
 259 **lines represent the 95% confidence interval of the fitted functions. Note: the 10.6%**  
 260 **case involves a two-stage fitting (the first for  $t \leq 230$  min with  $\eta_i = 0$  mm and  $\lambda_i = 46$**   
 261 **mm and the second for  $t > 230$  min with  $\eta_i = 3.8$  mm and  $\lambda_i = 92.6$  mm, see Table 2).**



262 **Figure 3. Plan view of the ripple morphology at the end of the experiments in the test**  
 263 **section.  $C_0$  is the initial bed clay content.**  
 264

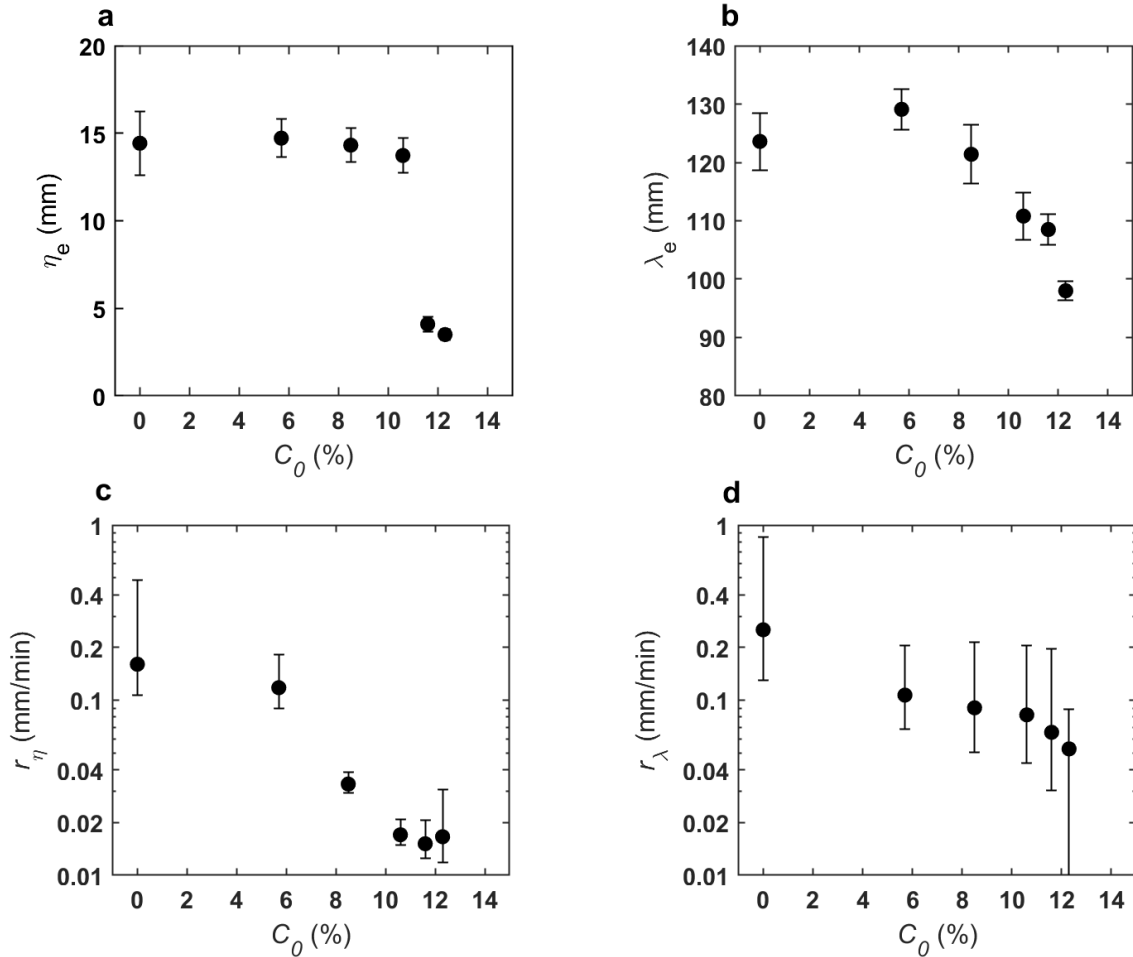
265 The ripples for the lowest bed clay content,  $C_0 = 5.7\%$  (Run 3, Channel 1), had a similar growth  
 266 rate to that of the clean-sand ripples in the first 50 min (Figure 2c, d). Thereafter, the ripple growth  
 267 rate reduced compared to the counterpart in clean sand, such that it took longer to reach  
 268 equilibrium: 125 min for the ripple height and 330 min for the ripple wavelength. The equilibrium  
 269 dimensions,  $\eta_e = 14.7$  mm and  $\lambda_e = 126.5$  mm, were similar to the clean-sand ripples, as was their  
 270 morphology, with two-dimensional ripples covering the bed (Figure 3b).

271 As  $C_0$  was increased,  $t_i$  increased from 60 min to 120 min (Figure 2e - l; Table 2). Increasing  $C_0$   
 272 also slowed the subsequent ripple development compared with the clean-sand case (Figure 2 e - l).  
 273 This is particularly true for  $C_0 = 10.6\%$ , where the ripple height and wavelength only grew to 3.9  
 274 mm and 96.2 mm at  $t = 170$  min, compared to 14.1 mm and 122 mm for the clean-sand ripples at  
 275 the same point in time. In the following hour these small ripples tended to be stable; Equations 3  
 276 and 4 also captured the growth trends well in height and wavelength in this stage (Figure 2g, h).  
 277 After  $t = 230$  min, the ripple height experienced a period of relatively rapid, yet gradually  
 278 decelerating, growth in the next approximately seven hours, reaching  $\eta_t = 11.5$  mm at  $t = 530$  min  
 279 and  $\eta_e = 13.7$  mm at  $T_\eta = 678$  min (Figure 2g; Table 2), which was similar to the equilibrium height  
 280 of the clean-sand ripples. Ripple wavelength reached equilibrium  $\lambda_e = 110.9$  mm at  $T_\lambda = 540$  min  
 281 (Figure 2h; Table 2). Not only the dimensions of the ripples were similar to the clean-sand ripples  
 282 for  $C_0 \leq 10.6\%$ , but these ripples were also two-dimensional, tended to be slightly asymmetric  
 283 with  $RSI \approx 1.3$ , and they had  $RS = 0.11-0.14$  (Figure 3c - d; Table 2).

284 The initial ripple height growth trends for the 11.6% and 12.3% cases were like their 10.6%  
 285 counterparts until  $t = 230$  min (Figure 2i, k). However, thereafter, the ripples experienced weak  
 286 growth in the remainder of the experiments and were unable to develop to sizes similar to the  
 287 clean-sand ripples, reaching  $\eta_e = 4.1$  mm and  $\eta_e = 3.5$  mm at  $T_\eta = 271$  min and  $T_\eta = 211$  min ( $r^2 =$

288 0.76 and 0.79), respectively (Figure 2i, k; Table 2). Wavelength development was also hindered  
 289 in these high clay content cases. For the 11.6% case, 280 min were required to reach  $\lambda_e = 108.5$   
 290 mm, whereas a longer period of 499 min was needed to reach a shorter  $\lambda_e = 98$  mm for the 12.3%  
 291 case. These differences in ripple dynamics, compared to the clean-sand ripples, were also reflected  
 292 in their geometry. For  $C_0 = 11.6\%$ , the ripples were quasi-2D, characterised by straight but  
 293 discontinuous crestlines, whereas barchan-shaped ripples with discontinuous crestlines were  
 294 observed for  $C_0 = 12.3\%$  (Figure 3e, f). Both these ripple types were more asymmetric, with RSI  
 295 = 1.5, and markedly flatter, with  $RS \approx 0.05$ , than the clean-sand ripples (Table 2).

296 Figure 4 illustrates the relationship between the initial clay content and the principal properties of  
 297 the equilibrium combined-flow ripples. The equilibrium ripple height was almost independent of  
 298 the initial clay content for  $C_0 \leq 10.6\%$ , at  $\eta_e \approx 14.4$  mm, whereas  $\eta_e$  collapsed to 3.5 mm at the  
 299 highest  $C_0$  of 12.3%, almost four times smaller than the clean-sand equilibrium height (Figure 4a).  
 300 The equilibrium wavelength was between 121.4 mm and 129.1 mm for  $C_0 \leq 8.5\%$ , and declined  
 301 linearly at higher  $C_0$  values, i.e., from 110.8 mm at 10.6% to 98 mm at 12.3% (Figure 4b). The  
 302 growth rate decreased gradually between 0% and 12.3% clay (Figure 4c, d). In the clean-sand run,  
 303  $r_\eta$  and  $r_\lambda$ , were 0.16 and 0.25 mm/min, respectively. At  $C_0 = 12.3\%$ , the growth rates were up to  
 304 an order of magnitude lower at  $r_\eta = 0.017$  mm/min and  $r_\lambda = 0.052$  mm/min. Based on an  
 305 equilibrium migration rate of 4 to 9 ripple crests/h (Fernández et al., 2022) and the range of ripple  
 306 wavelengths of 71 - 132 mm, gives a migration rate,  $m = 5 - 20$  mm/min. The migration rate is at  
 307 least one order of magnitude greater than the ripple height and wavelength growth rates, therefore  
 308 it is justified to use equations 7 and 8 for the transport rate of clay sediments out of the bed as the  
 309 ripples remained unchanged when moving one ripple wavelength.



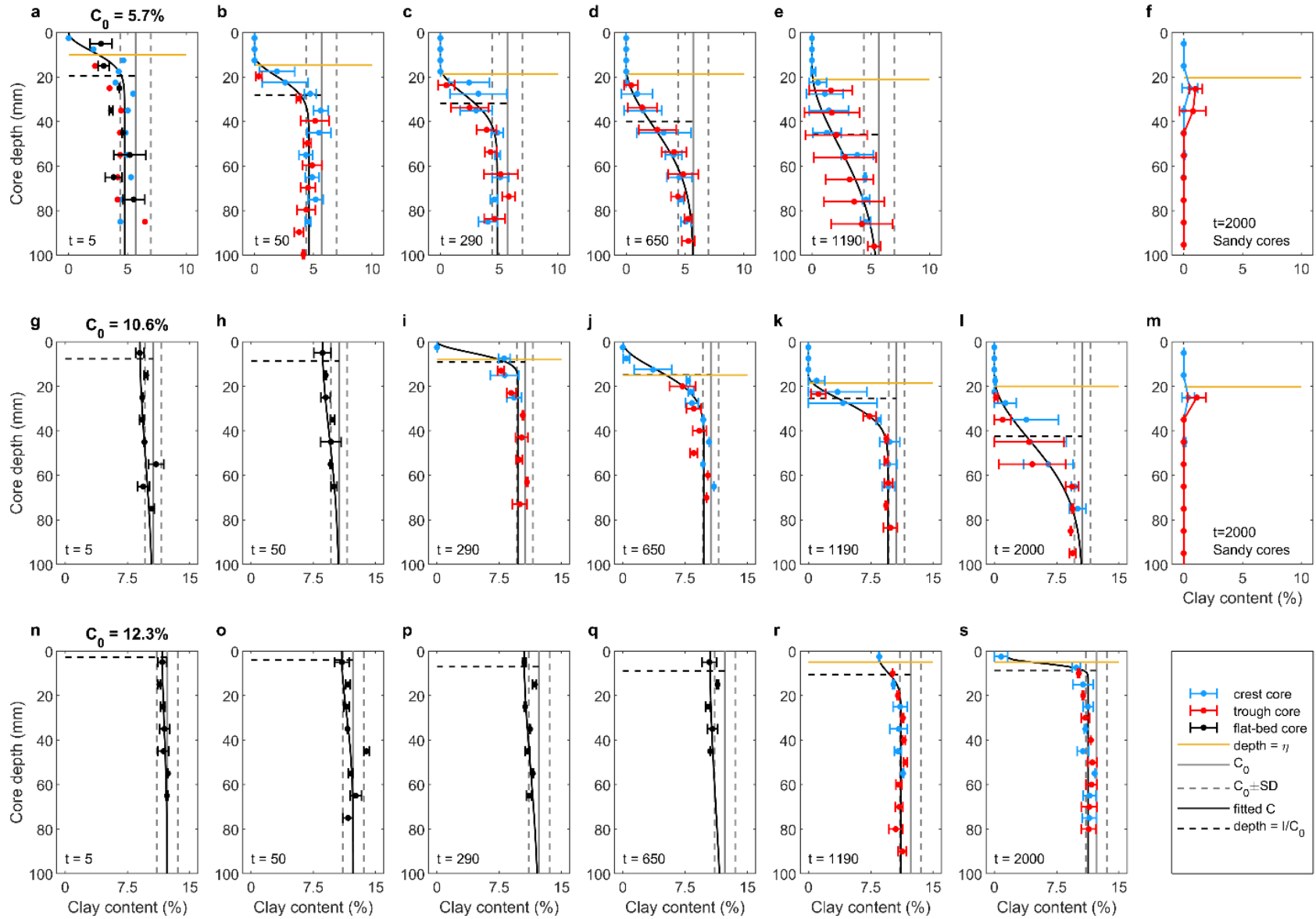
310 **Figure 4. Equilibrium combined-flow (a) ripple height and (b) wavelength, and**  
 311 **development rate of (c) ripple height and (d) wavelength against initial bed clay**  
 312 **content for all experiments. Black bars denote 95% confidence intervals, derived**  
 313 **from best-fit Equations 3 and 4.**  
 314

315 3.2. Change in bed clay content with ripple development

316 Figure 5 shows representative examples of the changes in bed clay content for different stages in  
 317 the development of the ripples for  $C_0 = 5.7\%$ ,  $10.6\%$ , and  $12.3\%$ , based on the grain-size analysis  
 318 of the sediment in the cores. The first profile for  $C_0 = 5.7\%$  was at  $t = 5$  min, when the bed was  
 319 partly flat and partly occupied by small ripples. In the upper 15 mm of the flat bed core (black dots  
 320 in Figure 5a), the clay content was about half of its initial value (grey vertical solid line in Figure

321 5a). Below this layer, the clay content increased with depth to its initial value (Figure 5a). The  
322 sand was free of clay below the crest of the small, 8 mm high, ripples, whereas a small amount of  
323 clay remained at the base of the ripple (blue dots in Figure 5a). There was clay loss in a 10-mm  
324 thick layer immediately below the ripple trough, with the clay content c. 60% lower than the initial  
325 value (red dots in Figure 5a). At  $t = 5$  min, the equivalent clean-sand depth  $d_c (= I/C_0)$  was  
326 approximately 20 mm (black horizontal dash line), which was much larger than the ripple height,  
327 suggesting that there was enough clean sand below the ripple trough to allow ripple growth. Below  
328 this layer, the clay content had remained close to its initial value (Figure 5a). Figures 5b – e  
329 illustrate the effect of ripple growth on the bed clay content. The clay content in the rippled part  
330 of the cores was zero, indicating that the winnowing of clay from the bed kept pace with the growth  
331 in ripple height. Furthermore, the thickness of the layer losing clay just below the ripple base  
332 progressively expanded downwards until it reached the pre-experiment value at the base of the  
333 deposit between 650 min and 1250 min. Consequently, the thickness of  $d_c$  continued to increase,  
334 reaching 45.8 mm by the end of the experiment (Figure 5e).

335



336 **Figure 5. Vertical profiles of clay content in cores collected from beds in the mixed sand–clay section with clay content of**  
337 **(a – e) 5.7%, (g – i) 10.6% and (n – s) 12.3%, and from end-of-experiment rippled beds in the clean sand section**  
338 **downstream of the three channels in (m) Run 2 and (f) Run 3. The grey vertical solid lines and the vertical dashed lines**  
339 **represent mean initial clay content and one standard deviation of the mean (See Figure S1). The black, blue, and red**  
340 **dots denote mean clay content below the active flat bed, ripple crest, and ripple trough, respectively. The black, blue,**  
341 **and red horizontal bars denote one standard deviation of the mean clay content. The solid black line is the fit to**  
342 **equation 9 (for 5.7% and  $t = 5$  min, the flat bed core is not used in the fit) and the dashed horizontal black line is  $d_c =$**   
343  **$I/C_0$ , the equivalent clean-sand depth. The yellow lines represent the ripple base and  $t$  is the time at which the core was**  
344 **taken is in min.**

345 Five minutes after the start of the run with  $C_0 = 10.6\%$ , the clay content in the top 10 mm of the  
346 flat bed core was lower than the initial value, but above 7.5%; this layer of slightly reduced clay  
347 content had expanded downward to c. 30 mm at  $t = 50$  min (Figure 5g, h). By  $t = 290$  min, the  
348 ripples contained 0% clay just below the ripple crest, but clay was retained at the ripple base. There  
349 was a relatively thin layer ( $\approx 10$  mm thick) showing a c. 30% reduction in clay content underneath  
350 the ripples, with  $d_c \approx \eta$  (Figure 5i). Compared to  $C_0 = 5.7\%$ , the sediment cores demonstrate a  
351 slower evolution towards fully developed sandy ripples in conjunction with a slower downward  
352 expansion of the layer with reduced clay content underneath the ripples (Figure 5i – l). By the end  
353 of the experiment, the thickness of the layer losing clay below the ripples was comparable with  
354 that of the 5.7% case, as  $d_c$  increased to 42.5 mm (Figure 5l).

355 The bed clay content for the 12.3% run was close to its initial value at  $t = 5$  min (Figure 5n). At  $t$   
356  $= 50$  min (Figure 5o), the upper 10 mm of the bed had lost a small amount of clay; ripples had not  
357 formed at this stage. Small ripples were present at  $t = 290$  and 650 min, but it was not possible to  
358 sample through the crests and troughs of these ripples. Bed clay content in the upper 10 mm had  
359 continued to decrease at these times (Figure 5p, q). Draining the tank at  $t = 1190$  min and  $t = 2000$   
360 min revealed small, c. 5 mm high, ripples. These ripples had retained 8.5% clay at  $t = 1190$  min,  
361 but only 0.8% at  $t = 2000$  min. While a thin layer of reduced clay content was present just below  
362 the base of the ripples (Figure 5r, s), the initial clay content was recovered at far shallower depths  
363 than for the 5.7 and 10.6% cases and  $d_c$  was close to  $\eta$ .

364 In the rippled-bed cases for all three initial concentrations (Fig.5b-e, i-l, r, s), fitting to a Gaussian-  
365 type function, equation 9, by optimising  $C_0$ ,  $C_s$ ,  $z_s$  and  $\alpha$  each time step (black line) provides a  
366 reasonable description of the data ( $R^2 \geq 0.74$ ). At the deepest point  $z = -b$  all clay contents are  
367 consistently within one standard deviation of the initial clay concentration (grey dashed lines).

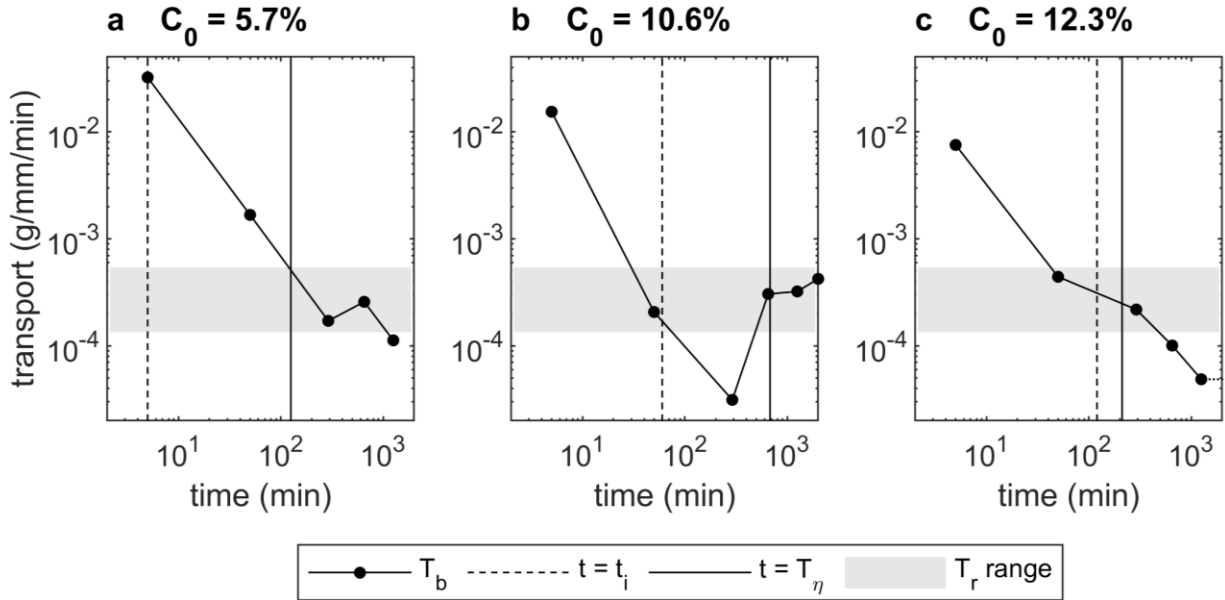
368 Figures 5f and 5m show vertical profiles of clay content collected from ripples in the downstream  
 369 clean-sand sections of the three channels in Run 2 and 3 at the end of the experiments. Both profiles  
 370 reveal clay-free ripples and a layer modestly enriched in clay below the base of the ripples. This  
 371 layer was c. 20 mm thick for  $C_0 = 5.7\%$  and c. 10 mm thick for  $C_0 = 10.6\%$ .

372 Figure 6 depicts the clay transport rates out of the bed,  $T_b$ , which were greatest at the beginning of  
 373 the experiment, where the bed was essentially flat. For  $C_0 = 5.7\%$  and  $10.6\%$ , the transport rates  
 374 then decreased as the ripples grew and tended to level off after ripples reached equilibrium (Figure  
 375 6a, b). For  $C_0 = 12.3\%$ ,  $T_b$  decreased throughout the experiment, with  $4.88 \times 10^{-5}$  g/mm/min at  $t =$   
 376 1190 min (Figure 6c). At the end of the experiment  $T_b$  even changed sign (dotted-line in Figure  
 377 6c), indicating that more clay entered the bed than left it through winnowing.

378 It is anticipated that loss of clay from the rippled beds is largely the result of winnowing from the  
 379 active layer ( $-\eta < z < 0$ ). For a triangular ripple containing a constant clay concentration,  $C_r$ , and  
 380 assuming that all clay present is removed after the passage of one ripple wavelength, this can be  
 381 expressed as a transport rate,  $T_r = \frac{1}{2}(1-p)\rho_s C_r m \eta$ , where  $m = 5 - 20$  mm/min. Conservatively  
 382 assuming a modest concentration,  $C_r = 1\%$ , and the minimum ripple height,  $\eta = 3.5$  mm, gives  $T_r$   
 383  $= 1.3 - 5.5 \times 10^{-4}$  g/mm/min. Figure 6 shows this range of  $T_r$  (grey shading area). It can be seen that  
 384  $T_r$  was comparable to  $T_b$  in the rippled beds, except at  $t = 5$  min when the bed was mostly flat,  
 385 implying that winnowing from the active layer can easily keep pace with the clay being lost from  
 386 the bed.

387 The cores collected from the clean-sand section downstream of the mixed sections have  
 388 demonstrated that clay can enter the bed through hyporheic processes (Figures 5f, m). Using  
 389 concentrations from Figures 5f, m instead of  $C_d$  in equation (7) allows a range for hyporheic  
 390 transport rates over the whole experiment for  $5.7\%$  and  $10.6\%$  ( $\Delta t = 1190$  and  $2000$  min) of  $-1.9$

391 and  $-0.7 \times 10^{-5}$  g/mm/min, i.e., into the bed, to be calculated. This is an order of magnitude smaller  
 392 than the conservative  $T_r$  estimate.



393

394 **Figure 6. Clay mass transport rate out of the bed,  $T_b$ , from equation 8, for  $C_0 = 5.7\%$**

395 **(a), 10.6% (b), and 12.3% (c). Grey shading corresponds to the range of estimated**

396 **clay mass transport rates in the active layer,  $T_r$ , due to winnowing induced by ripple**

397 **migration. Vertical dashed and solid lines correspond to the times of initiation and**

398 **full development for ripples ( $t_i$  and  $T_\eta$ ) and the dotted-line section of  $T_b$  for 12.3%**

399 **indicates where it goes negative.**

#### 400 **4. Discussion**

##### 401 **4.1. Ripple Development on Cohesive Substrates under Combined Flows**

402 The experimental results described in this paper illustrate the role of cohesive sediment in changing

403 the dynamics of combined-flow ripples by slowing the ripple growth rate (Figure 4c, d; cf. Baas

404 et al., 2013; Wu et al., 2018). For beds with  $C_0 \leq 10.6\%$ , the ripples developed to a comparable

405 equilibrium shape and size, with  $\eta_e \approx 14.4$  mm and  $\lambda_e \approx 123.8$  mm, but the cohesive forces caused

406 the equilibrium time to increase exponentially as  $C_0$  was increased from 0% to 10.6% (Table 2).  
407 These observations are consistent with the findings of Wu et al. (2018), who studied the  
408 development of wave ripples on sand beds with up to 7.4% kaolinite clay. However, Baas et al.  
409 (2013) described a small decrease in height and a constant wavelength of current ripples, as  $C_0$   
410 was increased from 0% to 12.6%, and a similar equilibrium time for all ripples independent of bed  
411 kaolinite content. The relatively short duration of 2 hours used in the experiments of Baas et al.  
412 (2013) may have prevented the best-fit equations (cf. Equations 3 and 4) from predicting  
413 sufficiently accurate equilibrium times, especially at  $C_0$  values between 7% and 12.6%. This  
414 viewpoint is supported by the experiments with mixtures of sand and biologically cohesive  
415 extracellular polymeric substances (EPS) of Malarkey et al. (2015), whose flow and sand  
416 properties were similar to those of Baas et al. (2013), but their runs lasted between 4 and 73 hours.  
417 Malarkey et al. (2015) concluded that current ripples developing on beds with EPS contents  
418 ranging from 0.016% to 0.125% reached similar equilibrium size and geometry as EPS-free current  
419 ripples, provided that sufficient time was allowed for their formation. 2D combined flow ripples  
420 developed in the present experiments, whereas 3D ripples were generated under similar combined  
421 flow velocities in Perillo et al.'s (2014b) experiments. This difference in ripple planform geometry  
422 is potentially attributable to the grain size used in the experiments; in the present experiment  
423 coarser sand,  $D_{50} = 450 \mu\text{m}$ , was used whereas  $D_{50} = 250 \mu\text{m}$  was used in Perillo et al.'s (2014b)  
424 experiments. O'Donoghue et al. (2006) found a tendency for 2D ripples to be generated when the  
425 grain size exceeded  $300 \mu\text{m}$ . The current component in the combined flow contributed to ripple  
426 asymmetry; RSI was around 1.4 in the present experiments, whereas ripples are more symmetric  
427 under wave-alone conditions, e.g.,  $\text{RSI} \approx 1.1$  in the experiments of Wu et al. (2018). This is also

428 in agreement with previous experimental studies on the influence of combined flow on ripple  
429 cross-section geometry (Perillo et al., 2014a).

430 The two strongest levels of bed cohesion ( $C_0 = 11.6\%$  and  $12.3\%$ ) used herein not only led to  
431 greatly reduced ripple dimensions ( $\eta_e < 5$  mm,  $\lambda_e < 108$  mm), but also to significantly different  
432 ripple geometries. At  $RS = 0.04$ , these small ripples resemble rolling-grain ripples without flow  
433 separation at the crest, as opposed to vortex ripples with flow separation that require  $RS > 0.1$   
434 (Miller and Komar, 1980). Rolling-grain ripples are associated with steady circulation cells on  
435 either side of the ripple crest (Hara and Mei, 1990), which drive sediment towards the crest,  
436 causing the ripple to grow until it is steep enough for flow separation and periodic vortex shedding  
437 to begin (e.g., van der Werf et al., 2008). Perillo et al. (2014b) identified small, two-dimensional  
438 rolling-grain ripples on clean sand beds under combined flows. However, the rolling-grain ripples  
439 at  $C_0 = 12.3\%$  in the present study were barchan-shaped (Figure 3f). It is likely that the stronger  
440 cohesion within the bed at  $C_0 = 12.3\%$  prevented these ripples from evolving into the two-  
441 dimensional ripples with discontinuous crestlines of  $C_0 = 11.6\%$  or even the straight-crested and  
442 continuous ripple trains of  $C_0 \leq 10.6\%$ . The fact that  $T_b$  changes sign in the  $C_0 = 12.3\%$  case in  
443 Figure 6c suggests that the ripples would be unlikely to evolve further, even if the experiment had  
444 been run for longer (Dallmann et al., 2021).

445 Previous experiments have found that clean-sand rolling-grain ripples are a transitional and  
446 unstable stage that evolve towards equilibrium vortex ripples (Scherer et al., 1999, Stegner and  
447 Wesfreid, 1999, Faraci and Foti, 2001). This transition is usually a rapid process. In the clean-sand  
448 experiments of Faraci and Foti (2001), rolling-grain ripples lasted less than 4 min before  
449 developing into vortex ripples when  $U_o = 0.43$  m/s. In the  $C_0 = 10.6\%$  case, however, the rolling-  
450 grain ripple stage was remarkably prolonged at around 290 min (Figure 2). The similarity between

451  $\eta$  and  $d_c$  in the sediment cores indicates that there was insufficient clean sand available beneath the  
452 active layer for ripple growth at  $t = 290$  min (Figure 5i). However, subsequently as  $d_c$  became  
453 larger, the ripples continued to grow and reached equilibrium as the clay at the base of the active  
454 layer dropped below 8%. A clay content of 8% may therefore be a threshold below which growth  
455 towards equilibrium clean-sand ripples is able to occur, and ripples develop separation vortices  
456 typical of vortex ripples. Bed clay contents above 8% thus prevent the circulation cells from  
457 supplying enough sand from the troughs to allow the ripples to grow and the flow to separate, so  
458 the rolling-grain ripples persist. This threshold was never passed in the 12.3% clay run, since the  
459 clay content below the base of the ripples remained at 10% or above consistently (Figure 5r, s),  
460 resulting in the persistence of rolling-grain ripples until the end of the experiment. Further research  
461 designed to quantify the clay-content threshold for the change from rolling-grain to vortex ripples  
462 under different forcing conditions is required to fully understand the influence of cohesive clay on  
463 ripple evolution and equilibrium ripple size and shape. This 8% threshold is consistent with Wu et  
464 al.'s (2018) experiments, since  $C_0 \leq 7.4\%$  for all of their experiments and no reduction in the wave  
465 ripple dimensions was found. Also interestingly, Baas et al. (2013) found a drastic reduction in the  
466 size of current ripples in runs with  $C_0 > 13\%$ , with heights and wavelengths lower than 5.5 mm  
467 and 80 mm. These smaller ripples were two-dimensional and flatter than the three-dimensional,  
468 linguoid, equilibrium clean-sand ripples (Baas et al., 2013). Most significantly, once formed these  
469 small current ripples were stable until the end of the experiments. The post-experiment clay content  
470 beneath the active layer was not measured by Baas et al. (2013), as visual observations suggested  
471 that the bed had remained relatively unchanged. Within the active layer, the bulk post-experiment  
472 clay content was measured,  $C_r$ , and found to be much reduced by efficient winnowing ( $0 \leq C_r \leq$   
473  $18\% C_0$ ). Thus it is likely that the clay content immediately below the active layer was between  $C_r$

474 and  $C_0$  (as in Figure 5). This would give a representative concentration of  $\frac{1}{2}(C_t+C_0)$  below the  
475 active layer or  $< 7.7\%$  for  $C_0 \leq 13\%$  and  $> 7.7\%$ , for  $C_0 > 13\%$ , which is very similar to the 8%  
476 threshold.

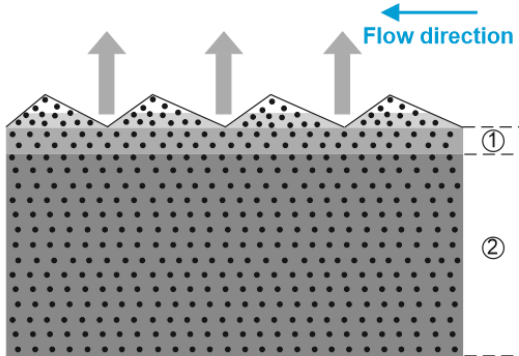
477 It is therefore concluded that two distinct types of equilibrium wave, current, and combined flow  
478 ripples are able to develop on mixed sand–clay beds, with the conceptual models of these two  
479 types of ripple development shown in Figure 7. If  $C_0 \leq C_t$ , the threshold bed clay concentration,  
480 relatively large equilibrium ripples, with dimensions and geometries comparable to clean-sand  
481 counterparts, are developed. These ripples experience similar development stages as those of  
482 clean-sand ripples, including incipient, growing, and equilibrium stages (Perillo et al., 2014b;  
483 Figure 7a – c), although the growth rate is lower than that of clean-sand ripples.

484 Relatively small and flat equilibrium ripples are generated as  $C_0 > C_t$  (Figure 7d – f). Incipient  
485 ripples that appear after an extended period of flat-bed conditions because of high bed cohesion,  
486 are unable to grow to large sizes because of a lack of clean-sand available from beneath the active  
487 layer (Figure 7e – f). The value of  $C_t$  can either be specified for the initial well mixed clay content,  
488  $C_0$ , in which case  $C_t = 10.6\%$ , or the clay content at the base of the active layer in which case  $C_t =$   
489 8%. Whereas the threshold for an initial well-mixed bed may be specific to the wave–current  
490 conditions, the 8% threshold at the base of the active layer appears to be more general.

$$C_0 \leq C_t$$

**a Incipient stage**

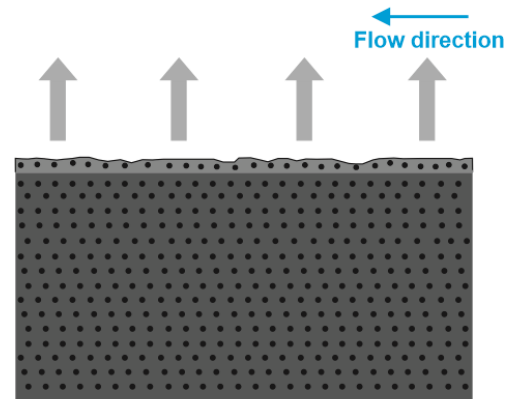
- Small dimensions
- Clean-sand below the small ripple crest
- Clay remained in the ripple base
- Relatively high clay winnowing rate



$$C_0 > C_t$$

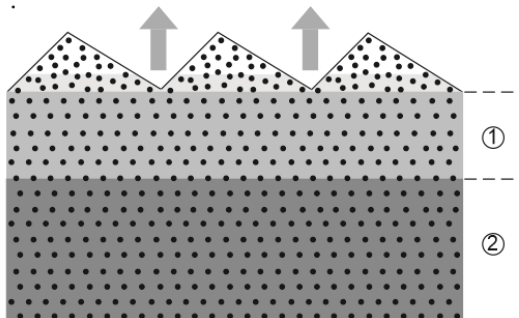
**d Bed remaining nearly flat**

- High bed cohesion to resist bed erosion



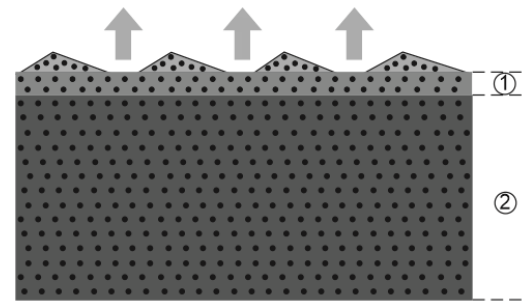
**b Growing stage**

- Growth rate decreases with increasing  $C_0$
- Evolution to sandy ripples
- Clay winnowing rate decreases



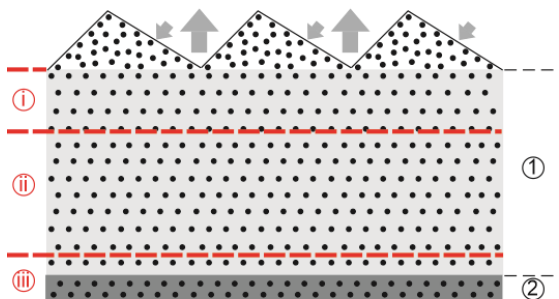
**e Incipient stage**

- Small and flat ripples with relatively high clay content
- High clay winnowing rate



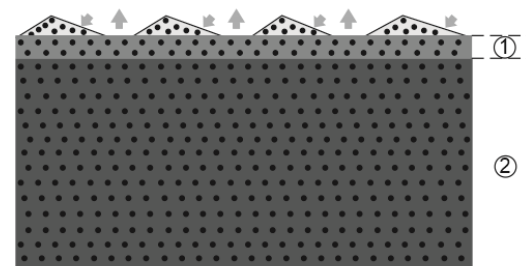
**c Equilibrium stage**

- Clean-sand ripples
- Similar dimensions and geometries as ripples from clean-sand bed
- Consistent low clay winnowing rate



**f Equilibrium stage**

- Small and flat ripples with small amount of clay
- Weak clay winnowing rate



① and ②: clay loss and inactive layer below combined-flow ripples  
 ①, ②, and ③: clay loss, clay-enriched, and inactive layer below wave ripples (Wu *et al.*, 2018)

492 **Figure 7. Conceptual models showing the development stages of (a - c) large and (d - f)**  
493 **small equilibrium ripples under currents, waves, and combined flows.  $C_t$ : threshold**  
494 **bed clay content. The horizons with different clay fractions are presented by**  
495 **different shades of grey. The grey arrows pointing upward represent clay**  
496 **winning and those pointing to the ripple stoss side represent clay entering into**  
497 **bed via hyporheic flow. Red dash lines represent boundaries of sediment layers**  
498 **below the wave ripples of Wu et al. (2018).**

#### 499 4.2. Deep Cleaning of Clay in Rippled Beds

500 Our sediment-core data confirm earlier findings that winnowing of fine, cohesive material, i.e.,  
501 clay and EPS, from the active layer leads to the transformation of a cohesive bed to sandy ripples  
502 (Baas et al. 2013; Malarkey et al., 2015; Wu et al., 2018). Furthermore, the present experimental  
503 results demonstrate that clay winnowing rates decrease as the ripples develop (Figure 6 and 7). In  
504 the incipient stage of ripple development, the clay in the active layer and immediately below it are  
505 easily winnowed as the ripples migrate, resulting in high clay winnowing rates (Figure 7a). As the  
506 ripples grow and clay in the active layer is exhausted, such that clay loss only occurs from below  
507 the ripple trough, the winnowing efficiency is significantly reduced (Figure 7c). For high clay  
508 content cases,  $C > 8\%$ , we infer that the weaker clay winnowing rate, after losing most of the clay  
509 contained in the active layer, is limited by stronger cohesion, beneath the ripples (Figure 7f).

510 Wu et al. (2018) identified layers enriched in clay relative to initial bed clay content below  
511 equilibrium wave ripples (Figure 7d). In the present experiments, clay did accumulate between 25  
512 and 35 mm in the sandy section downstream of the mixed sand–clay beds (Figure 5f, m). This  
513 provides further evidence that suspended clay can be carried into rippled beds by hyporheic flow,  
514 driven by pressure gradients between ripple troughs and crests (e.g., Huettel et al., 1996, Karwan

515 and Saiers, 2012, Dallmann et al., 2020). Clay probably also entered the rippled beds in the mixed  
516 sand–clay test section, as evidenced by the plateaus of increased clay content immediately below  
517 the ripple bases, e.g., between 22.5 and 45 mm and between 35 and 55 mm at the end of the 5.7%  
518 and 10.6% runs, respectively (Figure 5e, l). These depths are similar to the depths at which clay  
519 accumulated in the downstream sandy section and in the wave-ripple experiments of Wu et al.  
520 (2018; their figure 11), but there is still net clay loss at these depths in the mixed sand–clay test  
521 section. We infer that there is a dynamic balance between clay loss and gain below the base of the  
522 ripples. Clay gain by downward movement was higher than clay loss by upward winnowing below  
523 the base of the wave ripples, causing net clay accumulation at this depth, whereas winnowing-  
524 induced clay loss was dominant over hyporheic clay gain in the present combined-flow  
525 experiments, thus causing ‘deep cleaning’ of bed clay (Figure 7a - c). The fact that a Gaussian-  
526 type function describes the clay concentration below the active layer implies that the deep cleaning  
527 effect is diffusive in nature (e.g., Figure 5e and l). Winnowing was stronger under the combined-  
528 flow forcing herein than under the pure wave forcing of Wu et al. (2018), as illustrated by the  
529 active-layer winnowing transport rate estimate being an order of magnitude larger than the  
530 hyporheic transport rate estimate in the present experiments. Nevertheless, it is likely that  
531 eventually a balance is achieved between active layer winnowing and hyporheic processes as clay  
532 is used up in the active layer as ripples develop ( $C_r \rightarrow 0$ ), supported by the fact that  $T_b$  levels off  
533 over time and in the 12.3% case changes sign (Figure 6c).

534 It is well known that superimposed waves and currents generate high turbulence intensities and  
535 shear stresses in the wave boundary layer that are much greater than the sum of their constituents  
536 (Grant and Madsen, 1979, Mathisen and Madsen, 1996). Indeed, based on Malarkey and Davies’  
537 (2012) method, the maximum skin friction shear stress in the present experiments was 1.41 Pa, c.

538 40% higher than under wave-alone conditions with similar wave velocity amplitudes of Wu et al.  
539 (2018). This enhanced maximum shear stress, combined with the background turbulence  
540 associated with the current maintaining clay in suspension and far larger migration rates ( $5 \leq m \leq$   
541  $20$  mm/min), results in much stronger winnowing for wave–current conditions than wave-alone  
542 conditions. The stress in current-alone experiments of Baas et al.’s (2013) was the same as the  
543 wave–current mean stress (0.14 Pa) applied here, but the ripple migration rates were smaller ( $1 \leq$   
544  $m \leq 5$  mm/min versus  $5 \leq m \leq 20$  mm/min). Wu (2017) measured ripple migration rates under  
545 wave-alone conditions that were smaller than for the current ripples of Baas et al. (2013), i.e.  $1 \leq$   
546  $m \leq 2$  mm/min. The rate of winnowing of clay from the current ripples in Baas et al.’s (2013)  
547 experiments may therefore have been intermediate between those of Wu (2017) and the present  
548 study. Packman and Brooks (2001) quantified the relative importance of winnowing (turnover) to  
549 hyporheic pumping using the quantity  $U_p^* = pm/u_p$ , where  $p$  is the porosity ( $= 0.4$ ) and  $u_p$  is the  
550 pore water velocity (see Appendix A). Winnowing dominates when  $U_p^* \gg 1$  and hyporheic  
551 pumping dominates when  $U_p^* \ll 1$ . For the present experiments,  $u_p = 1.5$  mm/min and  $1.3 \leq U_p^*$   
552  $\leq 5.3$ , for Baas et al. (2013),  $u_p = 0.24$  mm/min and  $1.7 \leq U_p^* \leq 8.3$  and for Wu et al. (2018),  $u_p =$   
553  $1.7$  mm/min and  $0.24 \leq U_p^* \leq 0.47$ . Thus according to this parameter hyporheic processes are least  
554 important for the current-alone experiments of Baas et al. (2013) and the present experiments and  
555 most important for the wave-alone experiments of Wu et al. (2018). However, even in the wave-  
556 alone experiments winnowing still dominated in the active layer. Only the present wave–current  
557 experiments show the deep cleaning winnowing effect when winnowing is dominant. This is  
558 analogous to the ‘wave-pumping’ effect, that produces a deeper hyporheic exchange for wave–  
559 current conditions than wave-alone conditions when the flow is hyporheically dominated (Clark  
560 et al., 2019).

## 561 4.3. Implications for Natural Environments

562 The present experiments, supported by Baas et al. (2013) and Wu et al. (2018), show that ripple  
563 types change into one another across a narrow range of bed clay contents, suggesting a  
564 discontinuity in ripple dimensions and geometries that is not incorporated in mathematical  
565 predictors for bedform height and wavelength (e.g., Tanaka et al., 1996; Nelson et al., 2013).  
566 Because the large equilibrium ripples resemble clean-sand ripples as a result of highly effective  
567 clay winnowing, the application of these predictors may be extended from pure sand beds to  
568 weakly cohesive mixed sand–clay beds. However, these predictors need to be modified to capture  
569 the small equilibrium ripples that are stable only on strongly cohesive beds. This indicates that  
570 bedform predictors developed from clean-sand ripples are likely to overpredict ripple roughness  
571 for sand beds with a high bed clay content. Indeed, using  $k_s = 27.7\eta^2/\lambda$  (Li and Amos, 1998), where  
572  $k_s$  is the bed roughness due to form drag, the sudden reduction in ripple dimensions at  $C_0 > 10.6\%$   
573 (Figure 4a, b) causes the bed roughness to decrease by an order of magnitude. Brakenhoff et al.  
574 (2020) highlighted the fact that small changes in predicted form roughness could result in large  
575 changes in sediment transport rate predictions. The data in this study show that such errors may  
576 result from neglecting the profound effect of cohesive forces in mixed sand–clay beds, thus  
577 limiting the ability of models to accurately predict changes in the bed morphology of estuaries and  
578 coastal seas. The discontinuity between large and small combined-flow ripples was at an initial  
579 bed clay content of 10.6% and at a clay content of c. 8% below the base of the ripples. While it is  
580 expected that the 10.6% threshold, which relates to a well-mixed clay bed, is likely to be dependent  
581 on the maximum combined shear stress involved, the 8% condition appears to be more general as  
582 it concerns the dynamic nature of cohesive properties in the bed below the ripples. However, both  
583 thresholds will be affected by the additional presence of EPS-induced biological cohesion in  
584 sediment in the field (Baas et al. 2019), which has a stronger capacity to resist erosion compared

585 to physical cohesion; small proportions of EPS, of the order of 0.1%, are highly effective in  
586 hindering bedform evolution (Malarkey et al., 2015, Parsons et al., 2016). Indeed, Baas et al.  
587 (2021) observed a reduction in current ripple height on an intertidal flat during neap tides from c.  
588 20 mm to c. 10 mm for relatively low clay content between 2 and 5%, combined with EPS content  
589 between 0.05 and 0.08%. Nonetheless, the findings in this paper should act as a stimulus for further  
590 studies towards fully quantifying changes in ripple morphology as a function of hydrodynamic  
591 forcing and bed cohesion. This would also be helpful for designing the next-generation phase  
592 diagrams for combined-flow bedforms, which at present do not cover bed cohesion and therefore  
593 cannot predict the small equilibrium ripples found in this study (Dumas et al., 2005, Perillo et al.,  
594 2014a).

595 Our wave–current experiments show that an apparently stable cohesive mixed sand–clay bed can  
596 become unstable quickly through highly efficient clay winnowing (deep cleaning) far below the  
597 bed surface and the active layer,  $d_c \gg \eta$  (e.g., Figure 5e, l). This rapid change from a cohesive  
598 substrate to a mobile, predominantly sandy substrate is likely to occur on intertidal flats under  
599 storm-induced wave–current flows, as at the beginning of the Dee field campaign (Litchman et al.  
600 2018; Baas et al., 2021). The rapid change in bed stability may further challenge the modelling of  
601 sediment transport in estuaries, given that river flooding often goes hand in hand with storm events  
602 (e.g., Gong et al., 2007, Ralston et al., 2013). Such combined flows would not only lead to clay  
603 loss by winnowing under high maximum bed shear stress, but it may also lead to an increased  
604 supply into the estuary of suspended terrestrial clay as well as organic matter and toxic chemicals  
605 attracted to clay particle surfaces through physicochemical forces (Partheniades, 2009). These  
606 materials could become trapped in the estuary, especially during extended periods of calm  
607 conditions, given the slow deposit entry rates discussed by Dallmann et al. (2020). During

608 subsequent storms, however, the strong winnowing-induced, ‘deep cleaning’ effect is likely to  
609 release large volumes of clay, nutrients, and pollutants back into the water column over a short  
610 amount of time, with potentially severe impacts on the health of the estuarine environment. For  
611 example, a sudden, large release of nutrients may cause algal blooms, or ‘red tides’ (Brand et al.,  
612 2012), and a sudden, large release of contaminants causes near-instantaneous water pollution,  
613 threatening the ecological balance of estuarine and coastal environments and anthropogenic  
614 activities. The findings of this study are therefore also beneficial for the development of evidence-  
615 based water-quality regulations in estuaries.

## 616 **5. Conclusions**

617 The present experiments examined the importance of physical cohesion on the size and  
618 morphology of ripples generated by combined waves and currents. The experimental data illustrate  
619 that, with initial clay content,  $C_0$ , increasing from 0% to 12.3%, ripple height and wavelength  
620 development rates,  $r_\eta$  and  $r_\lambda$  decreased by one order of magnitude from 0.16 to 0.017 mm/min and  
621 from 0.25 to 0.052 mm/min, respectively. Clay transport rates out of the bed, as determined by  
622 sediment cores measured during the experiment, decreased during ripple development. The  
623 experimental results also revealed the development of two distinct types of equilibrium ripples on  
624 mixed sand–clay beds. For  $C_0 \leq 10.6\%$ , large two-dimensional, quasi-asymmetric equilibrium  
625 ripples developed, with equilibrium height and wavelength,  $\eta_e = 14.4$  mm,  $\lambda_e = 123.9$  mm, ripple  
626 symmetry index,  $RSI = 1.4$ , and ripple steepness,  $RS \approx 0.12$ . These geometric values are close to  
627 those of clean-sand ripples, because the winnowing of clay from the developing ripples at these  
628 low  $C_0$ -values was highly effective, typically resulting in 100% clay loss in the active layer.  
629 Relatively large clay transport rates out of the bed even after equilibrium resulted in clay  
630 winnowing extending far below the active layer, as demonstrated by the equivalent clean-sand

631 depth being far larger than the ripple height. This ‘deep cleaning’ of clay is probably attributable  
632 to higher bed shear stresses and migration rates under combined flow than under pure currents and  
633 pure waves. In contrast, high bed cohesion with  $C_0 > 10.6\%$  led to a discontinuity in equilibrium  
634 ripple height, generating small, flat, and more asymmetric equilibrium ripples, with  $\eta_e$  and RS  
635 collapsing to 4 mm and 0.04, respectively, but RSI increasing to 1.5. This bed-cohesion  
636 discontinuity is compounded by relatively small clay transport rates out of the bed, preventing the  
637 erosion of ripple troughs, and therefore limiting the sand supply needed for the growth towards  
638 larger clean-sand ripples. The 10.6% threshold in initial concentration coincides with an 8%  
639 concentration threshold at the base of the active layer that inhibits ripple development and is  
640 common to other experiments. The experimental findings re-emphasise the importance of  
641 including clay content in the bedform prediction of sediment transport models for muddy  
642 environments, such as estuaries. Moreover, combined wave–current conditions during storm  
643 events have the capacity to winnow large amounts of fine cohesive sediments from the bed, leading  
644 to bed instability and water pollution; which may have an impact on existing estuarine  
645 environmental regulations.

## 646 **Acknowledgments**

647 The authors acknowledge the enormous contributions of Brendan Murphy, whose help throughout  
648 the study made our setup, data collection, and clean-up efforts smooth and trouble-free. We  
649 acknowledge Oliver Dawes and the Hull Marine Laboratory at the University of Hull for their  
650 support in processing grain sizes with the Malvern Mastersizer 2000. We also acknowledge the  
651 extremely useful contributions of Ellen Pollard, Dr. Hachem Kassem, Prof. Stuart McLelland, Dr.  
652 Elena Bastianon, Dr. Anne Baar, Dr. Christina Roggatz, and Sojiro Fukuda during different stages  
653 of the experiments. Participation of XW, RF, JM and DP was made possible thanks to funding by  
654 the European Research Council under the European Union’s Horizon 2020 research and

655 innovation program (grant no. 725955). Participation of RF also supported by the Leverhulme  
 656 Trust, Leverhulme Early Career Researcher Fellowship (grant ECF-2020-679).

657 **Conflict of Interest**

658 The authors declare no conflicts of interest relevant to this study.

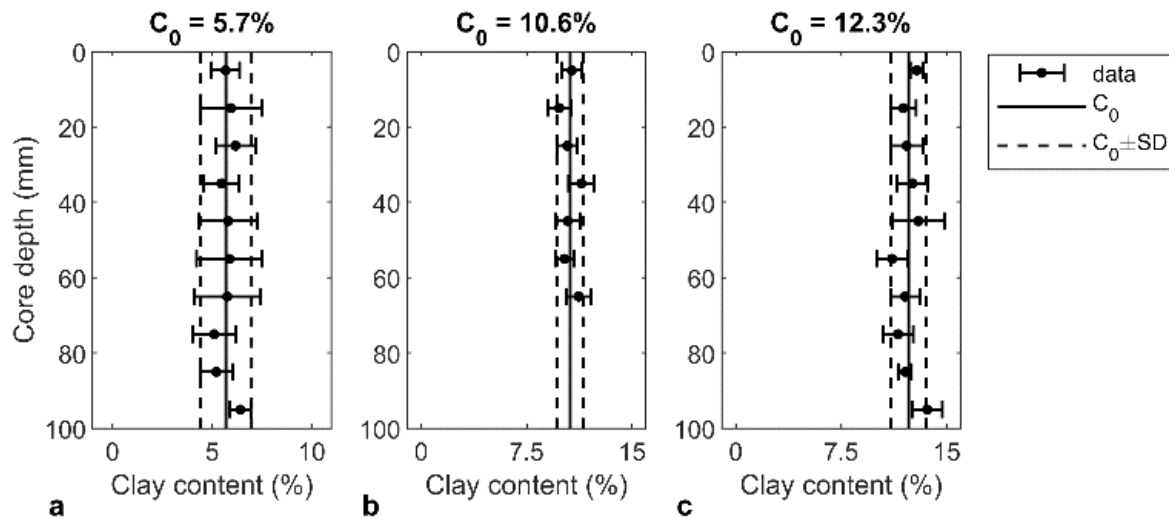
659

660 **Open Research**

661 Supporting data are available through figshare which is a free and open repository (Wu et al.,  
 662 2021).

663

664 **Supplementary materials**



665 **Figure S1. Initial clay content in the three experimental cases considered in Figure. 5 ( $C_0 =$**   
 666 **5.7, 10.6 and 12.3%) showing the data and one standard deviation at each level and the**  
 667 **mean and standard deviation over all depths.**

668

669 **Appendix A: Pore water velocity calculation**

670 The pore water velocity,  $u_p$ , which scales the hyporheic processes in the bed, can be calculated by  
 671 the method of Packman et al. (2000)

$$u_p = kKh_m \quad (A1)$$

672 where  $k = 2\pi/\lambda$ ,  $K = 600D_{10}^2$  is the hydraulic conductivity in mm/min,  $D_{10}$  is the 10-percentile of  
673 the grain-size distribution in mm,  $h_m = 0.14(U^2/g)(\eta/0.34h)^{3/8}$  is the half-amplitude dynamic head,  
674 and  $U$  is the root-mean square flow velocity (Precht and Huettel, 2003). For the present  
675 experiments,  $U = 0.31$  m/s,  $D_{10} = 0.3$  mm and  $u_p = 1.5$  mm/min, for Baas et al. (2013),  $U = 0.4$   
676 m/s,  $D_{10} = 0.072$  mm and  $u_p = 0.24$  mm/min and for Wu et al. (2018),  $U = 0.3$  m/s,  $D_{10} = 0.34$  mm  
677 and  $u_p = 1.7$  mm/min.

678 **References**

- 679 Baas, J. H. 1994. A flume study on the development and equilibrium morphology of current ripples  
680 in very fine sand. *Sedimentology*, 41, 185-209.
- 681 Baas, J. H. 1999. An empirical model for the development and equilibrium morphology of current  
682 ripples in fine sand. *Sedimentology*, 46, 123-138.
- 683 Baas, J. H., Baker, M. L., Malarkey, J., Bass, S. J., Manning, A. J., Hope, J. A., Peakall, J.,  
684 Lichtman, I. D., Ye, L. & Davies, A. G. 2019. Integrating field and laboratory approaches  
685 for ripple development in mixed sand–clay–EPS. *Sedimentology*, 66, 2749-2768.
- 686 Baas, J. H., Davies, A. G. & Malarkey, J. 2013. Bedform development in mixed sand–mud: The  
687 contrasting role of cohesive forces in flow and bed. *Geomorphology*, 182, 19-32.
- 688 Baas, J., Malarkey, J., Lichtman, I. D., Amoudry, L. O., Thorne, P., Hope, J. A., Peakall, J.,  
689 Paterson, D. M., Bass, S. & Cooke, R. D. 2021. Current-and Wave-Generated Bedforms  
690 on Mixed Sand–Clay Intertidal Flats: A New Bedform Phase Diagram and Implications for  
691 Bed Roughness and Preservation Potential. *Frontiers Earth Science*, 9, 747567.
- 692 Brakenhoff, L., Schrijvershof, R., Van Der Werf, J., Grasmeyer, B., Ruessink, G. & Van Der Vegt,  
693 M. 2020. From ripples to large-scale sand transport: The effects of bedform-related  
694 roughness on hydrodynamics and sediment transport patterns in delft3d. *Journal of Marine  
695 Science and Engineering*, 8, 892.
- 696 Brand, L. E., Campbell, L. & Bresnan, E. 2012. Karenia: The biology and ecology of a toxic genus.  
697 *Harmful algae*, 14, 156-178.
- 698 Cizeau, P., Makse, H. A. & Stanley, H. E. 1999. Mechanisms of granular spontaneous stratification  
699 and segregation in two-dimensional silos. *Physical Review E*, 59, 4408.

- 700 Clark, J. J., Qian, Q., Voller, V. R. & Stefan, H. G. 2019. Hyporheic exchange in a gravel bed  
701 flume with and without traveling surface waves. *Advances in Water Resources*, 123, 120-  
702 133.
- 703 Dallmann, J., Phillips, C. B., Teitelbaum, Y., Sund, N., Schumer, R., Arnon, S. & Packman, A. I.  
704 2020. Impacts of suspended clay particle deposition on sand-bed morphodynamics. *Water*  
705 *Resources Research*, 56, e2019WR027010.
- 706 Dallmann, J., Phillips, C. B., Teitelbaum, Y., Cifuentes, E. Y. S., Sund, N., Schumer, R., Arnon,  
707 S. & Packman, A. I. 2021. Bedform segregation and locking increase storage of natural  
708 and synthetic particles in rivers. *Nature Communications*, 12, 7315, doi: 10.1038/s41467-  
709 021-27554-4.
- 710 Dumas, S., Arnott, R. & Southard, J. B. 2005. Experiments on oscillatory-flow and combined-flow  
711 bed forms: implications for interpreting parts of the shallow-marine sedimentary record.  
712 *Journal of Sedimentary research*, 75, 501-513.
- 713 Faraci, C. & Foti, E. 2001. Evolution of small scale regular patterns generated by waves  
714 propagating over a sandy bottom. *Physics of Fluids*, 13, 1624-1634.
- 715 Fernández, R., Kassem, H., Wu, X. & Parsons, D. 2022. Changes in ripple migration rates and  
716 hydraulic resistance with increasing mud-to-sand ratios. *Prcoeedings of 39<sup>th</sup> IAHR world*  
717 *congress*, Granada, Spain, 19 – 24 June.
- 718 Gong, W., Shen, J. & Reay, W. G. 2007. The hydrodynamic response of the York River estuary  
719 to Tropical Cyclone Isabel, 2003. *Estuarine, Coastal and Shelf Science*, 73, 695-710.
- 720 Grant, W. D. & Madsen, O. S. 1979. Combined wave and current interaction with a rough bottom.  
721 *Journal of Geophysical Research: Oceans*, 84, 1797-1808.

- 722 Hara, T. & Mei, C. C. 1990. Centrifugal instability of an oscillatory flow over periodic ripples.  
723 *Journal of Fluid Mechanics*, 217, 1-32.
- 724 Healy, T., Wang, Y. & Healy, J.-A. 2002. *Muddy coasts of the world: processes, deposits and*  
725 *function*, Elsevier.
- 726 Huettel, M., Ziebis, W. & Forster, S. 1996. Flow-induced uptake of particulate matter in permeable  
727 sediments. *Limnology and Oceanography*, 41, 309-322.
- 728 Karwan, D. L. & Saiers, J. E. 2012. Hyporheic exchange and streambed filtration of suspended  
729 particles. *Water Resources Research*, 48.
- 730 Khelifa, A. & Ouellet, Y. 2000. Prediction of sand ripple geometry under waves and currents.  
731 *Journal of waterway, port, coastal, and ocean engineering*, 126, 14-22.
- 732 Lapotre, M. G., Lamb, M. P. & Mcelroy, B. 2017. What sets the size of current ripples? *Geology*,  
733 45, 243-246.
- 734 Li, M. Z. & Amos, C. L. 1998. Predicting ripple geometry and bed roughness under combined  
735 waves and currents in a continental shelf environment. *Continental Shelf Research*, 18,  
736 941-970.
- 737 Li, M. Z. & Amos, C. L. 1999. Field observations of bedforms and sediment transport thresholds  
738 of fine sand under combined waves and currents. *Marine Geology*, 158, 147-160.
- 739 Lichtman, I.D., Baas, J.H., Amoudry, L.O., Thorne, P.D., Malarkey, J., Hope, J.A., Peakall, J.,  
740 Paterson, D.M., Bass, S.J., Cooke, R.D. & Manning, A.J., 2018. Bedform migration in a  
741 mixed sand and cohesive clay intertidal environment and implications for bed material  
742 transport predictions. *Geomorphology*, 315, pp.17-32.

- 743 Malarkey, J., Baas, J. H., Hope, J. A., Aspden, R. J., Parsons, D. R., Peakall, J., Paterson, D. M.,  
744 Schindler, R. J., Ye, L. & Lichtman, I. D. 2015. The pervasive role of biological cohesion  
745 in bedform development. *Nature communications*, 6, 6257, doi: 10.1038/ncomms7257.
- 746 Malarkey, J. & Davies, A. G. 2012. A simple procedure for calculating the mean and maximum  
747 bed stress under wave and current conditions for rough turbulent flow based on method.  
748 *Computers & Geosciences*, 43, 101-107.
- 749 Mathisen, P. P. & Madsen, O. S. 1996. Waves and currents over a fixed rippled bed: 2. Bottom  
750 and apparent roughness experienced by currents in the presence of waves. *Journal of*  
751 *Geophysical Research: Oceans*, 101, 16543-16550.
- 752 Miller, M. C. & Komar, P. D. 1980. Oscillation sand ripples generated by laboratory apparatus.  
753 *Journal of Sedimentary Research*, 50, 173-182.
- 754 Myrow, P. M., Lamb, M. & Ewing, R. 2018. Rapid sea level rise in the aftermath of a  
755 Neoproterozoic snowball Earth. *Science*, 360, 649-651.
- 756 Nedwell, D., Parkes, R. J., Upton, A. & Assinder, D. 1993. Seasonal fluxes across the sediment-  
757 water interface, and processes within sediments. *Philosophical Transactions of the Royal*  
758 *Society of London. Series A: Physical and Engineering Sciences*, 343, 519-529.
- 759 Nelson, T. R., Voulgaris, G. & Traykovski, P. 2013. Predicting wave-induced ripple equilibrium  
760 geometry. *Journal of Geophysical Research: Oceans*, 118, 3202-3220.
- 761 O'Hara Murray, R., Thorne, P. & Hodgson, D. 2011. Intrawave observations of sediment  
762 entrainment processes above sand ripples under irregular waves. *Journal of Geophysical*  
763 *Research: Oceans*, 116.
- 764 O'Donoghue, T., Doucette, J., van Der Werf, J. J. & Ribberink, J. S. 2006. The dimensions of sand  
765 ripples in full-scale oscillatory flows. *Coastal Engineering*, 53, 997-1012.

- 766 Packman, A.I. & Brooks, N.H., 2001. Hyporheic exchange of solutes and colloids with moving  
767 bed forms. *Water Resources Research*, 37, 2591-2605.
- 768 Packman, A. I., Brooks, N. H. & Morgan, J. J. 2000. A physicochemical model for colloid  
769 exchange between a stream and a sand streambed with bed forms. *Water Resources*  
770 *Research*, 36, 2351-2361.
- 771 Parsons, D. R., Schindler, R. J., Hope, J. A., Malarkey, J., Baas, J. H., Peakall, J., Manning, A. J.,  
772 Ye, L., Simmons, S. & Paterson, D. M. 2016. The role of biophysical cohesion on  
773 subaqueous bed form size. *Geophysical research letters*, 43, 1566-1573.
- 774 Partheniades, E. 2009. *Cohesive sediments in open channels: erosion, transport and deposition*,  
775 Butterworth-Heinemann.
- 776 Pedocchi, F. & García, M. 2009. Ripple morphology under oscillatory flow: 2. Experiments.  
777 *Journal of Geophysical Research: Oceans*, 114.
- 778 Perillo, M. M., Best, J. L. & Garcia, M. H. 2014a. A new phase diagram for combined-flow  
779 bedforms. *Journal of Sedimentary Research*, 84, 301-313.
- 780 Perillo, M. M., Best, J. L., Yokokawa, M., Sekiguchi, T., Takagawa, T. & Garcia, M. H. 2014b. A  
781 unified model for bedform development and equilibrium under unidirectional, oscillatory  
782 and combined-flows. *Sedimentology*, 61, 2063-2085.
- 783 Precht, E. & Huettel, M. 2003. Advective pore-water exchange driven by surface gravity waves  
784 and its ecological implications. *Limnology and Oceanography*, 48, 1674-1684.
- 785 Ralston, D. K., Warner, J. C., Geyer, W. R. & Wall, G. R. 2013. Sediment transport due to extreme  
786 events: The Hudson River estuary after tropical storms Irene and Lee. *Geophysical*  
787 *Research Letters*, 40, 5451-5455.

- 788 Rubin, D. M. & Carter, C. L. 2005. *Bedforms 4.0: MATLAB code for simulating bedforms and*  
789 *cross-bedding*, US Geological Survey.
- 790 Scherer, M., Melo, F. & Marder, M. 1999. Sand ripples in an oscillating annular sand–water cell.  
791 *Physics of Fluids*, 11, 58-67.
- 792 Snelgrove, P. & Butman, C. 1995. Animal-sediment relationships revisited: cause versus effect.  
793 *Oceanographic Literature Review*, 8, 668.
- 794 Soulsby, R. 1997. *Dynamics of marine sands: a manual for practical applications*, Thomas Telford.
- 795 Soulsby, R. & Clarke, S. 2005. Bed shear-stress under combined waves and currents on smooth  
796 and rough beds (TR 137).
- 797 Southard, J. B. 1991. Experimental determination of bed-form stability. *Annual Review of Earth*  
798 *and Planetary Sciences*, 19, 423-455.
- 799 Stegner, A. & Wesfreid, J. E. 1999. Dynamical evolution of sand ripples under water. *Physical*  
800 *review E*, 60, R3487.
- 801 Tanaka, H. & Dang, V.T. 1996. Geometry of sand ripples due to combined wave–current flows.  
802 *Journal of waterway, port, coastal, and ocean engineering*, 122, 298-3000.
- 803 Van Der Mark, C., Blom, A. & Hulscher, S. 2008. Quantification of variability in bedform  
804 geometry. *Journal of Geophysical Research: Earth Surface*, 113.
- 805 Van Der Werf, J. J., Magar, V., Malarkey, J., Guizien, K. & O'Donoghue, T. 2008. 2DV modelling  
806 of sediment transport processes over full-scale ripples in regular asymmetric oscillatory  
807 flow. *Continental Shelf Research*, 28, 1040-1056.
- 808 Van Rijn, L. C. 2007. Unified view of sediment transport by currents and waves. I: Initiation of  
809 motion, bed roughness, and bed-load transport. *Journal of Hydraulic engineering*, 133,  
810 649-667.

- 811 Wengrove, M., Foster, D., Lippmann, T., De Schipper, M. & Calantoni, J. 2018. Observations of  
812 Time-Dependent Bedform Transformation in Combined Wave-Current Flows. *Journal of*  
813 *Geophysical Research: Oceans*, 123, 7581-7598.
- 814 Woodruff, J. D., Irish, J. L. & Camargo, S. J. 2013. Coastal flooding by tropical cyclones and sea-  
815 level rise. *Nature*, 504, 44-52.
- 816 Wu, X., Baas, J. H., Parsons, D. R., Eggenhuisen, J., Amoudry, L., Cartigny, M., Mclelland, S.,  
817 Mouazé, D. & Ruessink, G. 2018. Wave Ripple Development on Mixed Clay-Sand  
818 Substrates: Effects of Clay Winnowing and Armoring. *Journal of Geophysical Research:*  
819 *Earth Surface*, 123, 2784-2801.
- 820 Wu, X; Fernandez, R., Parsons, D. R., Baas, J. H., Malarkey, J. 2021. Laboratory measurement  
821 of wave–current ripple development [Dataset]. Figshare.  
822 <https://doi.org/10.6084/m9.figshare.16715578.v1>
- 823 Wu, X. (2017). Wave-induced ripple development in mixed clay-sand substrates. (unpublished  
824 PhD thesis). University of Hull, Hull, UK.